



# Development of a 5 fs laser system for the generation of ultra-short XUV radiation

---

A master thesis by Athanasios Lekosiotis

Advisors: Prof. Dimitrios Charalambidis

Dr. Paraskevas Tzallas

University of Crete – Physics Department

March 2017

MS<sub>c</sub> THESIS  
IN  
ATTOSECOND SCIENCE

Development of a 5 fs laser system for the  
generation of ultra-short XUV radiation

Defended by  
Athanasios Lekosiotis

COMMITTEE

---

Prof. Dimitrios Charalambidis – University of Crete  
Prof. Petros Rakintzis – University of Crete  
Dr. Paraskevas Tzallas – University of Crete

Date of the defense:  
29/03/2017

# Table of Contents

Abstract .....	1
Introduction .....	2
Thesis Layout .....	3
1. Operation principle of the hollow-core fiber 5-fs beam line .....	4
1.1 Key settings for efficient 5-fs pulse generation.....	6
1.1.1 Fiber Length & Diameter .....	6
1.1.2 Differential Gas Pumping.....	6
1.1.3 Coupling Lens & Fiber Entrance.....	8
1.1.4 Beam Lock System.....	10
1.1.5 Pulse Compression (Chirped Mirrors).....	12
2. Towards the development of a 5-fs beam-line .....	12
2.1 Primary Laser Source .....	13
2.2 Optical layout of the 5-fs beam line .....	14
2.2.1 Beam Stabilization System.....	15
2.2.2 Testing the beam stabilization system using photonic crystal fiber (PCF).....	16
2.2.3 Single-Shot FROG.....	20
2.2.4 FROG Calibration Procedure .....	23
3. Conclusion.....	29
4. Appendixes .....	30
Appendix A. Photonic Crystal Fibers.....	30
Appendix B. Nonlinear Dynamics .....	32
Appendix B1. Self-Phase Modulation (SPM) .....	33
Appendix B2. Self-Steepening .....	35
Appendix B3. Self-focusing .....	35
Appendix C. Super-Continuum Generation .....	36
Appendix D. Second-Harmonic Generation.....	37
Appendix E. FROG Calibration .....	38
5. Acknowledgements .....	38
6. References .....	39

**Abstract**

The aim of this thesis is the analysis and development of 5 fs IR laser pulses for purposes of generating XUV attosecond laser pulses for various ultrafast dynamics experiments. To achieve this, the Attosecond Science and Technology laboratory of FORTH-IESL provides a Ti:Sapphire laser system which produces 30 fs pulses of light. In order to reach the 5 fs regime, an experimental setup which includes a hollow core fiber and chirped mirrors will be used.

## Introduction

The generation of few-cycle laser pulses consists of challenging tasks in nonlinear optics. The demand for shorter pulses is consistent and desirable for many applications of physics, chemistry and biology. Furthermore, fundamental experiments with stabilized carrier envelope phase (CEP) rely on the generation of high-peak power few-cycle pulses. The process of super-continuum generation (SC) with the use of a hollow-core fiber filled with a noble gas of tuned pressure gradient accompanied with chirped mirrors for pulse temporal compression offers a powerful tool to produce ultra-short pulses. With this technique 5 fs pulses with hundreds of  $\mu\text{J}$  and several mJ can be generated at kHz and Hz repetition rates, respectively. [1].

Super-continuum is a broad spectrum generated through nonlinear optical effects (mainly self-phase modulation) in an optical fiber or bulk material by a high intensity propagating laser light. It was first discovered in bulk BK7 glass by Alfaro & Shapiro in 1970s [2]. Nonlinear optical effects arise when a dielectric medium is subjected to an intense field (i.e. high-power pulsed laser). Those effects usually result in the generation of new frequency components and thus increase the spectral bandwidth of the incident pulse. SC generation has numerous applications in fields like spectroscopy, pulse compression and the design of tunable femtosecond laser sources [3]. A pulse compression system is obligatory to reach the 5-fs regime and the chirped mirrors (CM) provide one. Chirped mirrors are dielectric mirrors frequently used for dispersion compensation in mode-locked lasers. The basic principle of their design is the variable Bragg wavelength within the structure so that light at different wavelengths penetrates to different depths experiencing different group delays [4].

The above technology was extensively used for the generation of CEP stable few-cycle IR laser pulses, which have been used for time-resolved experiments and isolated XUV attosecond pulse generation with the quest for high energy of the driver pulse being at the focus of investigation. Due to gain narrowing limiting the minimal duration achieved at mJ pulse energies to  $\sim 20$  fs, spectral broadening of the amplified pulses by nonlinear processes provides the generic solution. Many experimental studies published were designed towards the aim of generating sub 10-fs systems. The corresponding setups revolve around the same principle of spectral broadening the input pulse with a fiber, post-compress it with chirped mirrors and eventually characterize the output pulses using a diagnostic device like FROG or SPIDER. Most of these studies output energies of at most 1 mJ due to the poor or none CEP stabilization methods used that provide little or none control on the fluctuations of the beam's coupling with the fiber.

*F. Lucking et al.* [37] studied the CEP offset effects on the output spectrum and produced 3.9 fs transform-limited pulses with pulse energies up to 2.1 mJ at the output of the fiber. A useful setup of an ultra-short laser system was built by *Bohle et al* [35]. In this study, CEP-stable 4-fs near-IR pulses with 3 mJ of energy were generated by focusing circularly polarized 8 mJ pulses at 1 KHz repetition rate in a differentially pumped 2 meter long hollow fiber. The main findings of these studies in combination with the very rich literature on this research section are going to be used in the present work for the development of the 5-fs beam line.

## Thesis Layout

The present thesis is organized in the following way: in *Section 1*, the operation principle of a system generating 5 fs IR pulses is presented alongside some key aspects that should be taken under consideration for this kind of systems as derived from corresponding literature. These include selecting the proper fiber and chirped mirrors, compensating the self-focusing effect induced by the intensity of the pulses, differentially pumping the fiber and developing a beam stabilization system for an efficient beam-fiber coupling. In *Section 2*, the main part of the thesis unfolds with an analysis of the under-development 5-fs pulse system in the Attosecond Science and Technology laboratory of FORTH-IESL. A detailed description entails the layout segments that were completed during this work. These are the beam stabilization system with its testing procedure and a FROG device with its calibration procedure. Finally, this section contains a brief description of the primary laser source that shall be used as input for the 5-fs pulses.

After the *Conclusion* remarks, *Appendix A* provides some basic information about photonic crystal fibers, *Appendix B* presents the nonlinear dynamics taking place inside the fiber such as self-phase modulation and self-focusing. In *Appendix C*, a brief summary of super-continuum generation advancements is presented with some of its modern-day applications. In *Appendix D*, the second-harmonic generation (SHG) is discussed and in *Appendix E* a theoretical FROG calibration procedure is presented. The thesis is concluded with the *Acknowledgements* and *References* sections.

## 1. Operation principle of the hollow-core fiber 5-fs beam line

The 5-fs pulse regime requires the employment of a spectral broadening mechanism (hollow-core fiber) and a pulse compressor (chirped mirrors) alongside a Ti:sapphire CPA laser system that provides the input beam. These three parts' characteristics can heavily influence the ultra-short pulse output. For the description of the operation principle of the 5-fs beam line that is going to be developed in Attosecond Science & Technology lab of FORTH-IESL institute, I will use the experimental set-up described in ref. [35] and shown in Figure 1.

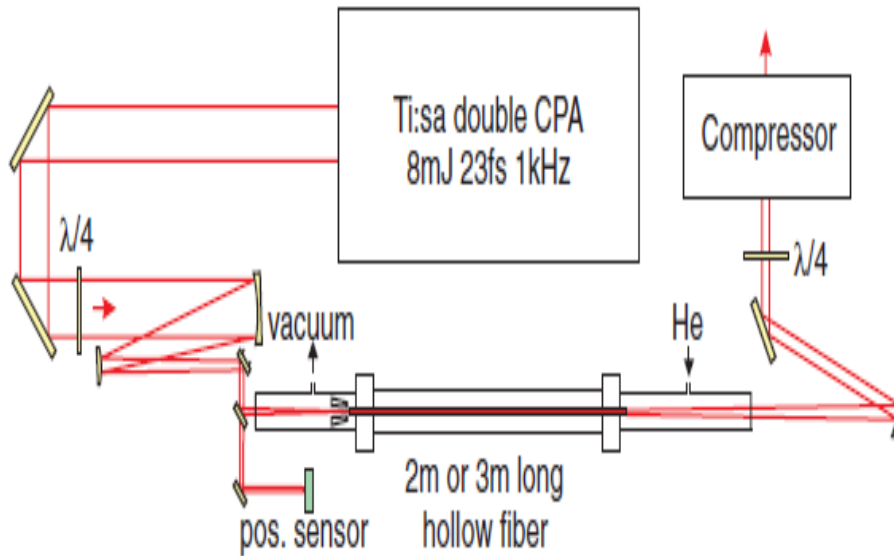


**Figure 1.** Model layout of the setup to be arranged in our lab for the generation of 5 fs laser pulses, from ref. [35].

A Ti:Sapphire CPA system of 8mJ, 23fs pulses running at 1 kHz was used for the input laser beam. Its pulses sustained a polarization rotation with a quarter-wave plate to a circular polarization state and were focused on a 2m long hollow fiber with 450  $\mu\text{m}$  of inner diameter supplied with a variable Helium gas input at the exit side of the fiber. Self-phase modulation (SPM – see Appendix B1) spectrally broadens the pulse inside the fiber and the output of the fiber after being collimated with a mirror is sent to the chirped mirror compressor for a pulse compression to sub-10 fs duration.

The setup includes the installation of a fused silica taper (not shown in the figure) and a gradient pressure operation of the capillary by controlling the input Helium gas density. These segments prevent possible damage at the entrance of the fiber due to pulse's high peak power and intensity. Also, the use of a circular polarization has proved to increase the fiber's transmission by around 20% compared to the linear polarization for similar spectral broadening due to reduced fluctuations at the coupling point between the pulse and the fiber's entrance [35]. A feedback system with a position sensor is installed just before the fiber entrance to overview the beam's position and its stability. An uncertainty of 20  $\mu\text{m}$  RMS of the beam's coupling was achieved in this setup. The pulses were compressed with a set of chirped mirrors (placed in the compressor region) inducing a negative chirp of 500  $\text{fs}^2$  group-

delay dispersion (GDD) value to compensate the positive chirp induced by the beam's propagation inside the fiber's gas and by the optics used beforehand. The output pulses were measured with a single-shot Second Harmonic Generation (SHG) FROG with a 5  $\mu\text{m}$  thick BBO crystal as the second-harmonic generator. The retrieved pulses exiting the chirp mirrors compressor are shown in Figure 2.

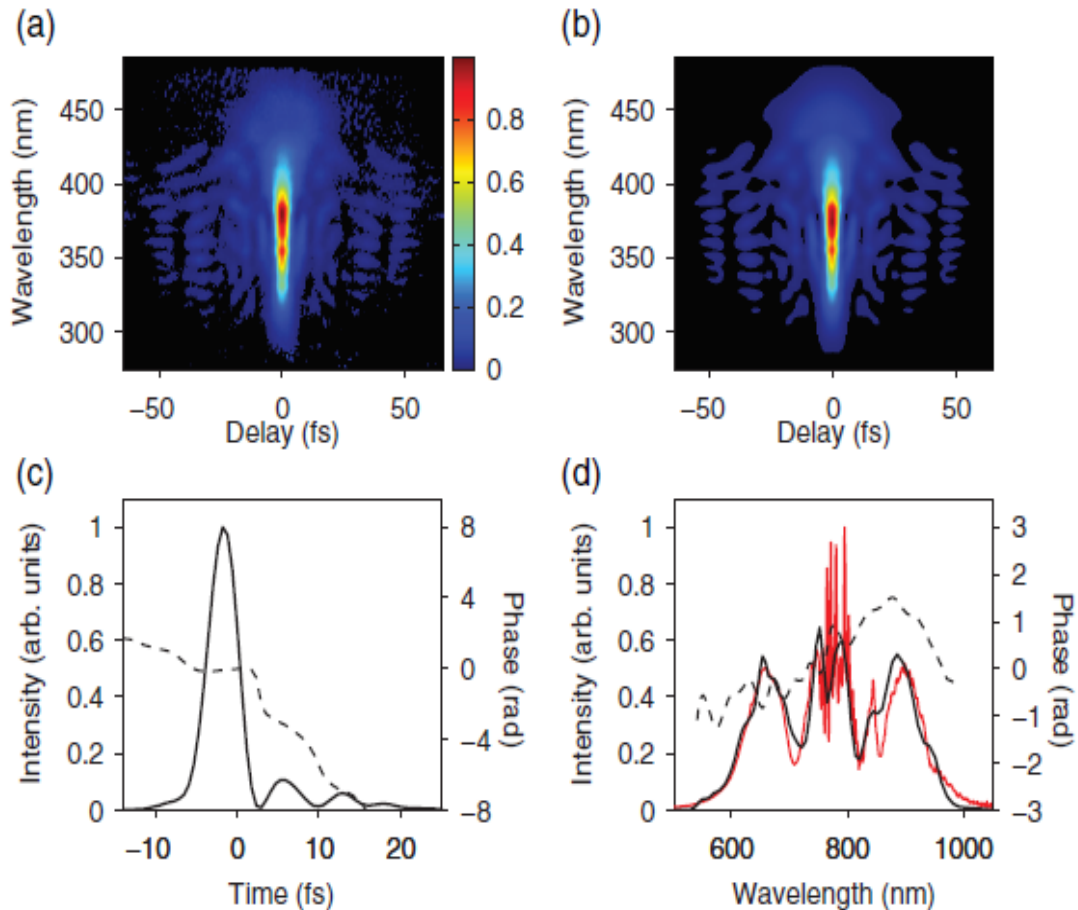


**Figure 2.** SHG-FROG measurements a) Experimental FROG trace, b) Retrieved FROG trace c) Retrieved temporal shapes, d) Retrieved spectral shapes. Dashed lines represent the phases while red line shows the spectrometer's measurement. From ref. [35].

FROG results show excellent agreement between the measured trace and the retrieved one for the electric field under study (Figure 2a, 2b). The temporal profile of the pulse was 4.27 fs (Figure 2c) and its spectral bandwidth spans from 500 nm to 1000 nm which corresponds to over-octave spanning spectra (Figure 2d). The spectral phase was smoothed by the chirp mirrors compressor. The Fourier transform limited pulse-duration of the spectrum is 2.6 fs corresponding to a single optical cycle which indicates even better results could be obtained with a matching set of chirped mirrors which would eliminate the total GDD induced by the fiber and the optics included and further smooth the output pulse spectral phase.

## 1.1 Key settings for efficient 5-fs pulse generation

The setup integrates many optimization segments for an efficient sub-10fs laser system. Although some already mentioned above, a detailed overview will be given in this section.

### 1.1.1 Fiber Length & Diameter

The fiber length and inner diameter of the waveguide are crucial to the generated pulse. The peak power of the input pulse is proportional to the effective fiber length and the waveguide's mode-area. The two criteria for successful spectral broadening concern the avoidance of self-focusing and photoionization procedures (see Appendix B3) showcasing limitations on pulse power and peak intensity, respectively. These limitations induce upper limits on these parameters, so critical power ( $P_{cr}$ ) and threshold intensity ( $I_{th} = P_{cr}/A_{eff}$ ) are defined,

$$P_{cr} = \frac{\lambda}{2\pi n_2} \quad (1)$$

In Equation 1,  $\lambda$  denotes the central wavelength,  $n_2$  the nonlinear refractive index of the medium and  $A_{eff}$  the effective mode area of the waveguide ( $\sim$  square of fiber's inner diameter). We also define the B-integral as the accumulated nonlinear phase from pulse propagation inside the fiber:

$$B = \frac{2\pi}{\lambda} \int_0^L n_2(z) I(z) dz = \frac{2\pi}{\lambda} n_2 I L_{eff} \quad (2)$$

Applying the power and intensity limitations in the B-integral, it depends only in waveguide geometry.

$$B \leq \frac{\lambda L_{eff}}{A_{eff}} \quad (3)$$

With  $L_{eff}$  denoting the effective interaction length in the fiber. In order to increase the power coupled in the fiber while maintaining the same spectral broadening, it concludes from Equations 2 and 3 that for high peak power, up-scaling of the effective waveguide length and inner diameter is required. This scaling law hints that long capillaries with large inner diameters provide more power coupled into the fiber and a larger bandwidth on the output. This will result on temporally shorter pulses.

### 1.1.2 Differential Gas Pumping

Noble gases like helium or neon deliver the low nonlinearity ( $n_2$ ) and the high ionization thresholds ( $I_{th}$ ) defined as necessary by the scaling law of the B-integral (Equation 2) when increasing the peak power of the pulse, but the achievable output energy is limited to order of 1 mJ. A major advancement of this problem was the differential pumping mode installation instead of a static filled mode. *J. S. Robinson et al.* [34] in 2006 compared the two modes of pumping and published the results.

With input laser pulses of 30-fs and 700  $\mu$ Joules energy, a neon-filled hollow fiber of 250  $\mu$ m inner diameter was pumped. The principle of the differential pumping is a gas injection in the exit end of the fiber while vacuuming the fiber entrance. This leads to a pressure gradient along the fiber. The removal of the gas at the entrance fiber window reduces ionization effects and allows constant energy transmission. The

coupling between the input pulse and the fiber ceases to be dependent on gas pressure and pulse's intensity permitting consistent coupling conditions for a broad range of pressures. It is at the end of the waveguide that the excessive nonlinear interaction takes place but this is an area where no significant losses are expected [35]. The comparing spectra for various gas densities are shown below for both statically filled (SF) and differentially pumped (DP) modes of operation.

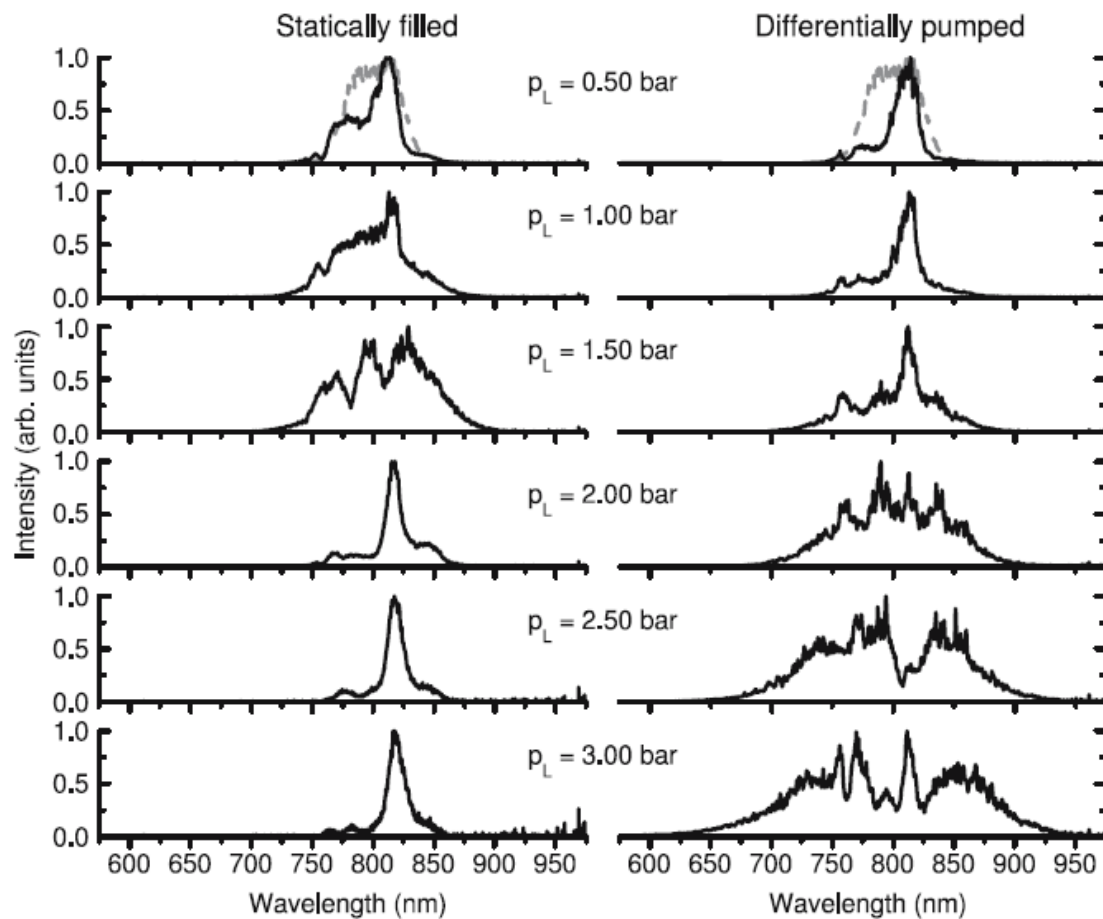


**Figure 3.** Super-continuum spectra after the hollow fiber for statically-filled (SF) mode (left) and the differentially pumped (DP) mode (right). From ref. [34].

Up until  $P = 1.5$  bar the SF mode generates broadened spectra compared to the DP mode, since the latter is affected by the low gas densities. However, when increasing the gas pressure the SF mode experiences losses and reduced energy is coupled while DP spectra continue to augment. At a pressure of 3 bars, the DP mode delivers almost octave-spanning spectra. The derived spectra for each gas pressure pumped in the fiber are the outcome of the energy coupling efficiency. A generic insight is also attained by the pressure relative to the transmission percentage as a validation for the generated spectra.

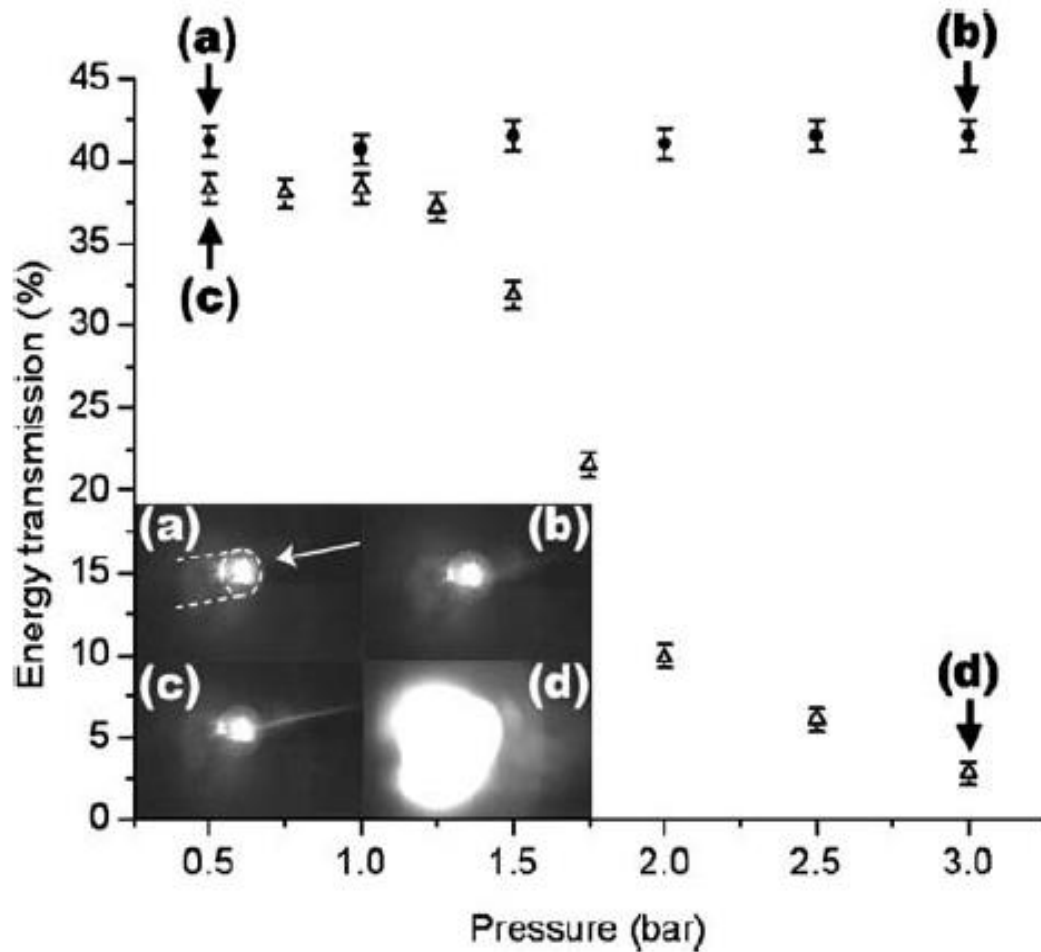


**Figure 4.** Comparison of the energy transmission for the SF mode (triangles) and the DP mode (circles) for various input gas pressures. Inset contains the CCD images of light coupled in fiber's hole points comparing the focal spot size for DP mode (a,b) and SF mode (c,d), for low pressures (a,c) and high pressures (b,d) respectively. From ref. [34].

The energy transmission drop of SF mode due to ionization defocusing at the fiber entrance and the simultaneous constancy of DP mode for the increasing gas pressure values confirm the supremacy of the DP mode. The ionization defocusing increases the focal spot size and the coupling efficiency is reduced. This can be seen from the corresponding CCD images of the beam's spot size obtained just before the fiber's entrance window displayed on the inset of Figure 4. The SF mode invokes aberrations (tracks of ionization) on the beam even for low pressures (Figure 4c). Increasing the gas pressure, light scatters up to the outer fiber diameter (Figure 4d). This behavior is not true for the DP mode which exhibits a well-coupled beam both for low pressures (<1 bar, Figure 4a) and for higher pressures (~3 bars, Figure 4b).

### 1.1.3 Coupling Lens & Fiber Entrance

When a laser beam with power  $P$  and beam radius  $w$  propagates in a nonlinear medium of thickness  $d$  and nonlinear index  $n_2$ , the focal length of the Kerr lens is inversely proportional to pulse's power

$$f = \frac{\pi w^4}{4n_2 d} \frac{1}{P} \quad (4)$$

This phenomenon called Kerr-lens effect becomes important for high given pulse power. Due to Kerr-lens effect induced at the focusing lens, used to couple light into the fiber hole, its focal length shortens by an amount relative to the magnitude of the effect. As a result, lens' optimal position needs to be decided for absolute distance compensation.

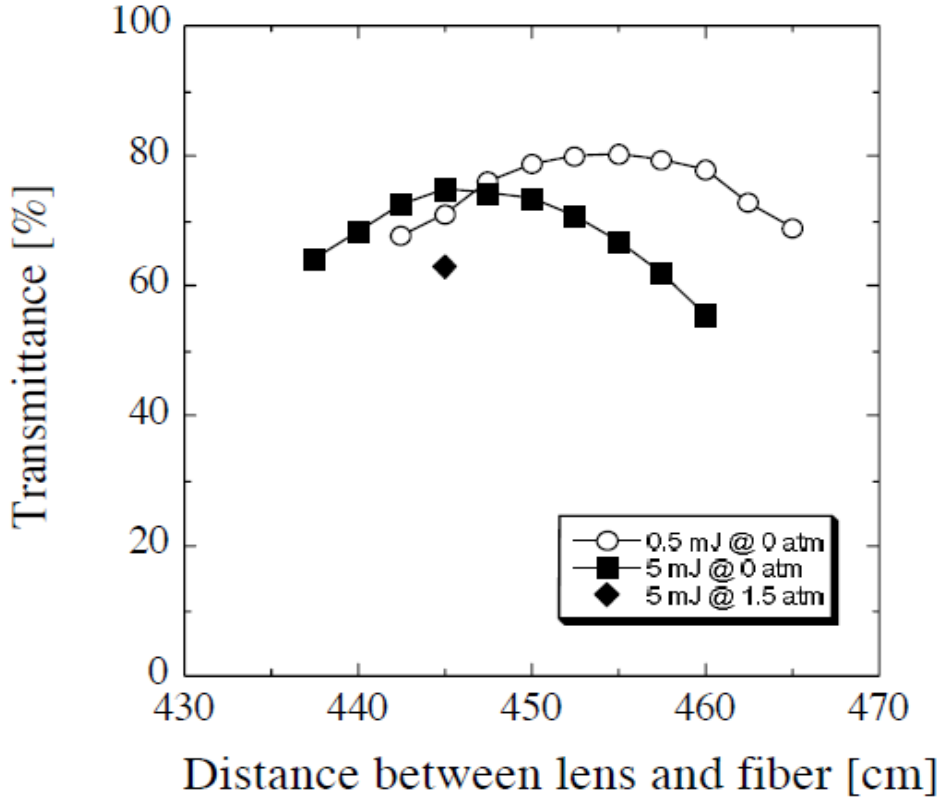


**Figure 5.** Measured transmittance for variable distance between an  $f = 4.5\text{m}$  focusing lens & fiber's entrance window. From ref. [18].

*Bohman et al.* [18] in 2008 studied this issue testing various lens positions relative to the fiber's entrance for input energies of 0.5 mJ and 5 mJ in vacuum and 5 mJ at neon pressure at 1.5 atm using an  $f = 4.5$  focusing lens. As seen in Figure 5, the optimal distance between the lens and the fiber alters up to 10 cm for varying input energies and seems independent of the gas pressure applied once the energy throughput is fixed. Neglecting the Kerr-lens effect for fixed pulse energies and gas pressures could decrease transmittance efficiency up to 20%.

Finally, the beam diameter must be set to 65% of the hollow fiber's diameter for maximal coupling efficiency [16]. Larger beams would not couple as efficiently reducing the overall transmission.

### 1.1.4 Beam Lock System

The most crucial aspect of the setup's efficiency as might have already been understood is the optimal beam coupling into the waveguide. Focusing the beam on the fiber's entrance can be highly unstable and more elegant systems are required to secure minimal fluctuations and constant spectral broadening for super-continuum spectra. Towards this direction, home-built feedback systems with beam locking properties are developed.

The setup from ref. [35] used for the operation principle description included a position sensor acting as a feedback system and achieving 20  $\mu\text{m}$  rms uncertainty on fluctuations but ultimately higher stabilizations can be attained with more complex systems like the model built by *T. Kanai et al.* [36] in 2008 accomplishing a feedback stabilization system of 1  $\mu\text{m}$  rms uncertainty. This system composed mainly of two Position-sensitive detectors (PSDs) in a two-loop fashion; one for feedback stabilization and one for monitoring control, a proportional-integral-derivative controller (PID) which is a feedback calculative mechanism that retrieves the signal sent by the PSD minimizing error values during calculations and a piezo-driven mirror with electric actuators. The PSD receives the input signal and transfers it to the PID circuit which performs the stabilization control through the piezo-driven mirror. The mirror eventually actuates the beam direction control.

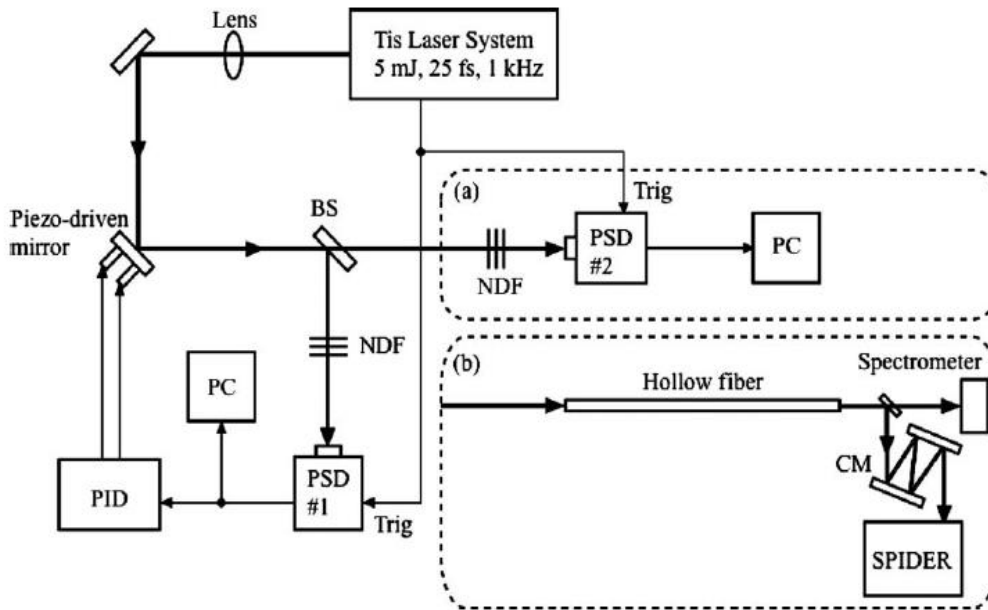


**Figure 6.** Schematic of the experimental setup for beam stabilization. PSD (position-sensitive detector) #1 is used inside the feedback loop for stabilization and PSD #2 (monitor loop a) is used for monitoring the beam quality outside the feedback loop. Rectangle (b) replaces monitor loop (a) once a stabilized beam-line is secured and setup proceeds to the ultra-short pulse generation measured with SPIDER. BS: beam-splitter, PC: personal computer, PID: proportional-integral-derivative controller, NDF: neutral density filters, CM: chirped mirrors. From ref. [36].

The layout of this stabilization system is given in Figure 6. Two PSDs are installed; one (PSD #1) for the feedback loop and one (PSD #2) for a general overview and evaluation of the beam stabilization system outside the loop. Distances between beam-splitters (BS) and PSDs were adjusted to be equal ( $\sim 3\text{m}$ ). Neutral

density filters (NDFs) are installed before each PSD for beam attenuation. After stabilization, the evaluation loop (Figure 6a) is replaced with the ultra-short pulse compression setup (Figure 6b) to test the stabilization results on the output pulses characterized with SPIDER.

The innovative operation of this stabilization system lies on the installment of the signal processing circuit (PID) which holds the signal value sent by the PSD sensor since the sensor itself remains inactive during the shot-to-shot time period. Thus, this incorporation allows for high repetition rate pulsed laser systems to be monitored. In this study, a 1 kHz CPA system was used. Below lie the beam fluctuations derived by PSD #1 before and after the appliance of the feedback loop.

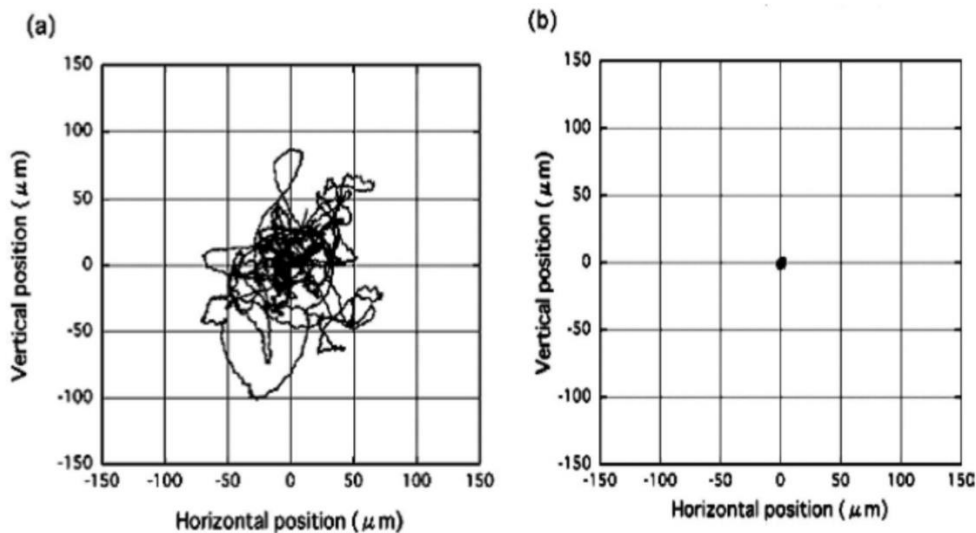


**Figure 7.** Fluctuations observed at PSD #1 a) without the feedback control and b) with feedback control. From ref. [36].

Beam fluctuations without the feedback control reach 30 rms horizontally and 42 rms vertically while feedback control reduces them to 1 rms horizontally and 1.1 vertically which is comparable to the accuracy of the differentially pumped 500  $\mu\text{m}$  hollow core fiber used for spectral broadening. The spectral intensity distributions for pulse compression without the feedback control and with it are presented in Figure 8a and 8b, respectively. Higher coupling power is observed for the latter case.

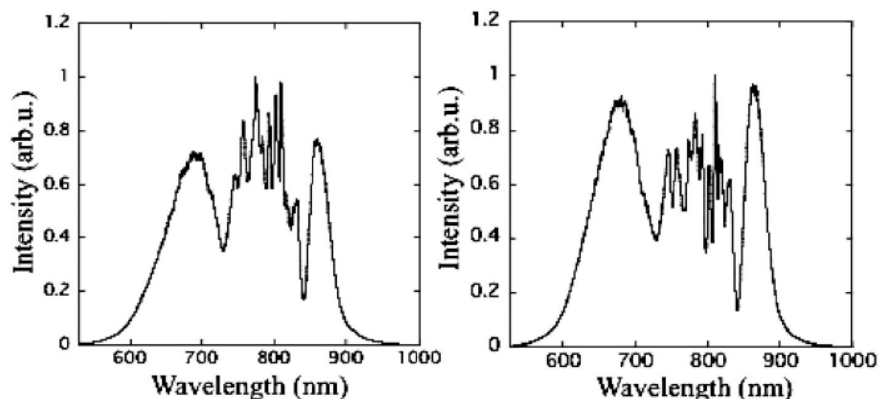


**Figure 8.** Output spectral profiles without (left) and with (right) feedback control. From ref. [36].

### 1.1.5 Pulse Compression (Chirped Mirrors)

Chirped mirrors are dielectric dispersive mirrors often employed for the generation of ultra-short laser pulses. Their principle is that the Bragg wavelength is gradually increased along the mirror structure, so they induce their inherent negative group delay dispersion (GDD) to the propagating pulse [4]. In practice it means that longer wavelength penetrate furthest in the mirror structure, experiencing larger group delay (see Figure 9).

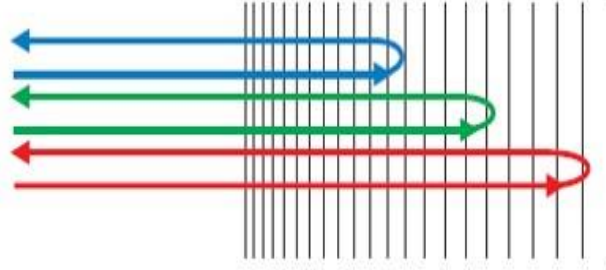


**Figure 9.** Principle operation of chirped mirrors. The longer the wavelength (red beam) the more it penetrates further in the mirror structure (black parallel lines) than the shorter ones (blue beam, green beam) so that longer wavelengths experience larger delays.

Propagation through various optics and interaction with the gas medium inside the fiber induce positive group delay dispersion (GDD) to the input pulse which should be compensated by chirped mirrors with an inherent negative GDD of the same absolute value in order to reach an ultra-short Fourier transform-limited pulse. This total induced GDD can be extracted from the spectral phase of the retrieved pulse on the output of the hollow core fiber. Main contribution to the spectral phase originates from material dispersion rather than the self-phase modulation (SPM) induced dispersion. Therefore, an increased gas density inside the fiber determines a limited portion of the total GDD introduced. This is convenient for generation of laser systems with variable duration just by alternating the gas pressure, setting both energy and alignment fixed.

## 2. Towards the development of a 5-fs beam-line

The generation of 5 fs pulses through a long hollow core fiber and a chirped mirror compressor is currently under process in our laboratory following the arrangement of ref. [35]. Due to time limitations, only certain parts of this setup were completed. These parts will be transferred and installed integrally during the ongoing theoretical and experimental process until its fulfillment.

The completed parts include; I) the FROG device for the spectral phase retrieval of the super-continuum and the eventual temporal duration measurement of the output pulse from the compressor. II) The beam stabilization system, required for efficient coupling between the input laser pulse and the hollow core fiber. Apart from these, an arrangement of an oscillator delivering the input pulses coupled in a small photonic crystal fiber was constructed to get a first glimpse on super-continuum spectra and test the beam stabilization system.

The analytical study and experimental aspects of the completed segments along with an initial projection of the complete-to-be hollow-core fiber setup are listed in following sections. The experimental process of this work was conducted in

the Attosecond Science and Technology Laboratory in the Institute of Electronic Structure & Laser Foundation for Research & Technology Hellas (I.E.S.L – FO.R.T.H), in Crete.

### 2.1 Primary Laser Source

A reliable tool to reach few-cycle regime is a sub-30 fs laser system with long-term CEP stability and energy output on the order of several mJoules. The beam of this laser system will provide the input for the spectrally broadened and afterwards compressed pulse in our home-built experiment.

## 30-fs Ti:Sapphire laser system

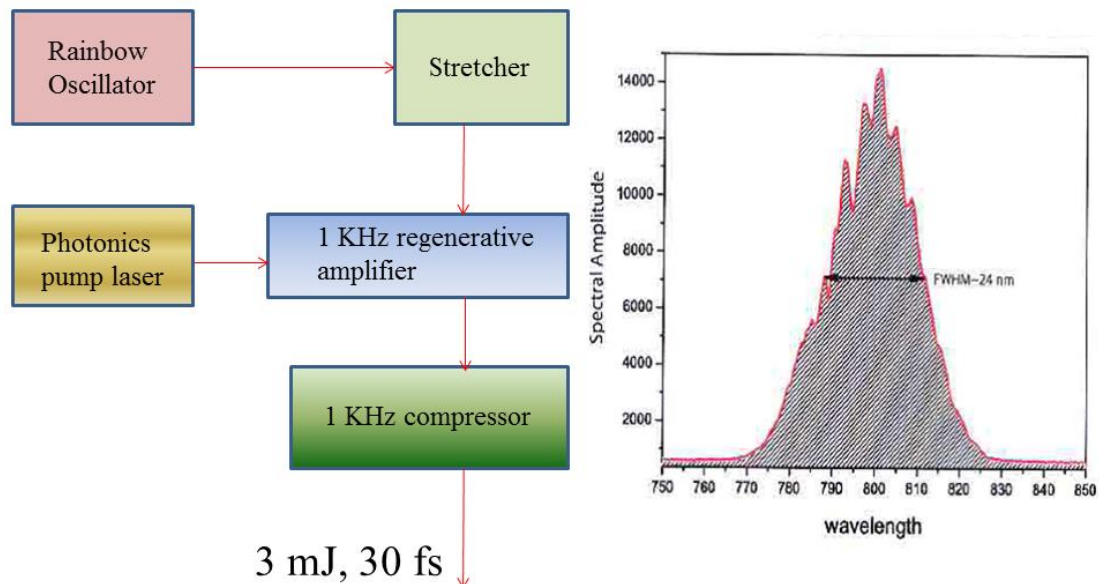


**Figure 10.** Laboratory’s Ti:Sapphire femtosecond laser at 1 KHz repetition rate delivering 30-fs pulses with 3 mJoule/pulse energy (left). Spectral distribution at the output of the kHz laser system (right).

The laboratory operates a femtosecond Ti:Sapphire amplified laser system of 30 fs output pulses. It constitutes of a Rainbow oscillator, a stretcher, a 1 kHz regenerative amplifier which is pumped by a Photonic Industries laser, producing a beam at 1 KHz repetition rates after the compressor. The pulse has a central wavelength of 800 nm and an energy output of 3mJoule/pulse. The spectral bandwidth after the compressors is about 24 nm as depicted in Figure 10.

## 2.2 Optical layout of the 5-fs beam line

The output pulse of the KHz laser system (30-fs pulse duration) will be coupled into a pressure-gradient hollow core fiber of 280  $\mu\text{m}$  of inner diameter and 1 meter long length (Optoelectronics Research Center, Southampton University) for an efficient spectral broadening of the pulse to reach the 5-fs regime.

The setup (Figure 11) will also include a set of chirped mirrors for pulse compression after the fiber, a beam stabilization system to improve the coupling efficiency and a FROG device to characterize the broadened pulse before the chirped mirrors and the compressed pulse afterwards. FROG retrieved spectral phase of the fiber's output pulse will point out the exact amount of chromatic dispersion compensation needed by the chirped mirrors to deliver close to Fourier transform limit 5-fs pulses.

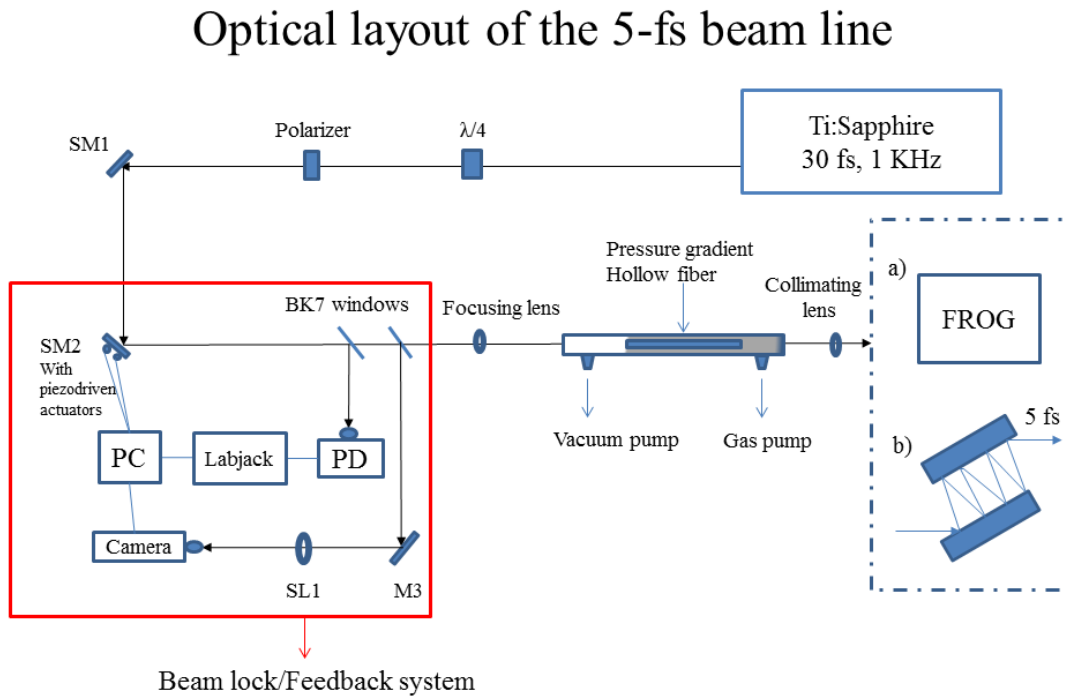


**Figure 11.** Optical layout of the 5-fs beam line. Red rectangle embeds the components of the constructed beam lock system with feedback control. Blue dashed rectangle embeds the setups used after the super-continuum generation; a) a FROG device to measure the spectral phase of the broadband pulse b) a set of chirped mirrors to compensate the chromatic dispersion defined by FROG's measurements that compresses the pulse down to 5-fs. SM1-2: steering mirrors, PD: quadrant photodiode, Labjack: data acquisition device running as analog to digital converter for PD's four optical channels, PC: personal computer, M3: mirror, SL1: spherical mirror.

In the diagram, two steering mirrors (SM1, SM2) are used to align the beam parallel to the optical axis of the hollow-core fiber. Before them, a polarizer and a half-wave plate ( $\lambda/2$ ) is placed to act as a variable power attenuator for the input pulse to prevent fiber damage during the alignment. After the alignment, we can replace the half-wave plate with a quarter-wave plate ( $\lambda/4$ ) so as to induce circular polarization. Circularly polarized pulses, as has been discussed previously, have the benefit of

diminishing the optical Kerr effect, increasing the ionization threshold [33] and generally provide a better stabilization of the beam compared to the linearly polarized pulses.

The hollow core of the fiber is exploited in a pressure gradient scheme. The fiber will be gas-filled preferably with a noble gas like Helium or Neon. The entrance of the fiber however, is vacuumed and as a result the self-focusing effect is prevented and the energy transmission remains constant (no losses to higher-order modes) [34]. After the spectral broadening of the pulse inside the hollow-core fiber mainly due to self-phase modulation (SPM) effects, a collimating lens focuses the beam at the entrance of the FROG device. The spectral profile of the pulse after the fiber is a super-continuum with a spectral phase distribution induced by the pulse's propagation in the gas medium of the fiber and the optics. Flattening the spectral phase can be achieved by the chirped mirrors in the compressor. A FROG measurement of the induced chirp after the output of the fiber will provide the exact GDD required for dispersion compensate. A suitable set of chirped mirrors will compress the pulse down to 5-fs close to the transform limit. The compressed pulse shall be characterized by the same FROG device.

### 2.2.1 Beam Stabilization System

A coupling lens that will be placed about 1 meter before the fiber's entrance will be used to focus the beam right at the fiber's entrance hole. As these focusing conditions can influence (due to beam pointing instabilities) the coupling of the laser beam with the fiber hole, a beam lock system has been developed that would relocate the beam straight to the entrance facet of the fiber and lock this position throughout the experiment.

The referenced beam stabilization system [36] consisted of two Position Sensing Detectors (PSDs) to obtain the pulse signal; one inside the feedback loop and one outside the loop as a monitoring scope, an analog Proportional-integral-derivative controller (PID) to perform the feedback control and a piezo-driven mirror with electric actuators. Our home-built stabilization system is based on the same loop principle with a quadrant photodiode (PD) acting as the feedback loop detector, a camera for the monitoring scope outside the feedback loop and a Labjack device acting as the corresponding PID circuit. Labjack is a data acquisition device that reads the signal sent by the detector and converts it to digital values while maintaining an error-minimizing approach.

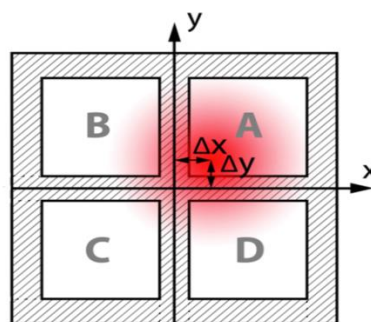


**Figure 12.** Quadrant Photodiode (PD) cross section used for centering the beam. PD contains four optical areas (A, B, C, D) enabling spatial beam mapping with  $\Delta x$ ,  $\Delta y$  corresponding to deviations from x and y axis respectively.

To insert the feedback control system in the setup, a BK7 window is used that sends a small fraction of the beam (around 3%) to the photodiode (PD) which is a quadratic sensor. The PD's photocell features four optically active areas labeled A, B, C, D oriented as seen in Figure 12. These areas constitute the four channels that output the obtained signal in the form of A+B, B+C, C+D and A+D. Once a beam hits the PD photocell, the signal measured for one channel will most likely be uneven compared to the rest of the channels due to the beam's random distribution (as is the case in Figure 12). Centering the beam would require a uniform signal distribution meaning that all four PD channels must obtain the same signal from the beam so the beam axis deviations ( $\Delta x$  and  $\Delta y$  in Figure 12) are as close to zero as possible. In order to perform this deviation-minimizing task, four BNC connectors (each corresponding to a different channel) are plugged between the PD's channels and the Labjack's Analog-to-Digital ports. The four signals (photocurrents) are therefore converted through Labjack to their equivalent voltage values with Labjack running signal conversion in a repeated fashion to secure high accuracy.

The digital output of the Labjack is then fed to a Python code which scans for the beam's optimal position relatively to the PD. The programming commands dictate the two-dimensional movement of the second steering mirror (horizontally and vertically) through the two piezo-linear electric actuators implemented on it. Their step resolution is less than 30 nm and they provide the set-and-forget stability meaning that they lock their positions even with no power applied. Once the proper increments have been made and the PD center is retrieved, the four-channel voltages return equal values ordering the program to save position and close. The auto-steering system will be successful provided that a proper manual collimation has already been made so small increments are required for the optimal beam centering.

A second BK7 window was placed just before the fiber's entrance and sent another 3% of the beam to a spherical lens (SL1) that projects on the camera a magnifying cross section of the fiber's hole with  $\mu\text{m}$  sensitivity. This allows for both a quick and intuitive way to locate the beam relative to the fiber's hole and a reference check on the auto-steering beam lock system.

### **2.2.2 Testing the beam stabilization system using photonic crystal fiber (PCF)**

The operation check of the home-built beam stabilization system was necessary before its installation on the main hollow fiber experiment. Together with the chance to get a glimpse on super-continuum generation, were the motives behind the construction of a compact setup with a short (12 cm long) photonic crystal fiber (Figure 13, Appendix A) called Femtowhite. The fiber was pumped by the MIRA 60-fs pulses and the output pulses were measured with a spectrometer.

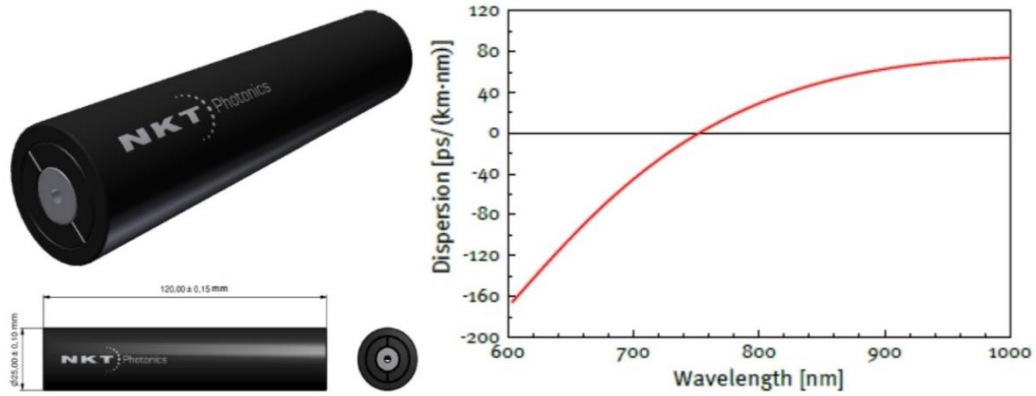


**Figure 13.** 3D, 2D and cross-sectional view of the 12 cm long PCF (left) and its dispersion for various input laser wavelengths (right). Its zero-dispersion wavelength (ZDW) is located around 750 nm.

Femtowhite, manufactured by NKT Photonics, Inc. is a polarization maintaining PCF with a zero-dispersion wavelength (ZDW, Appendix A) at 750 nm and a core diameter of 1.8  $\mu\text{m}$ . The PCF arrives with two x20 microscope objectives used to couple the input beam on the entrance of the fiber and for super-continuum collimation on the output of the fiber. Its pumping with the laser pulse requires a setup like the one shown in Figure 14.

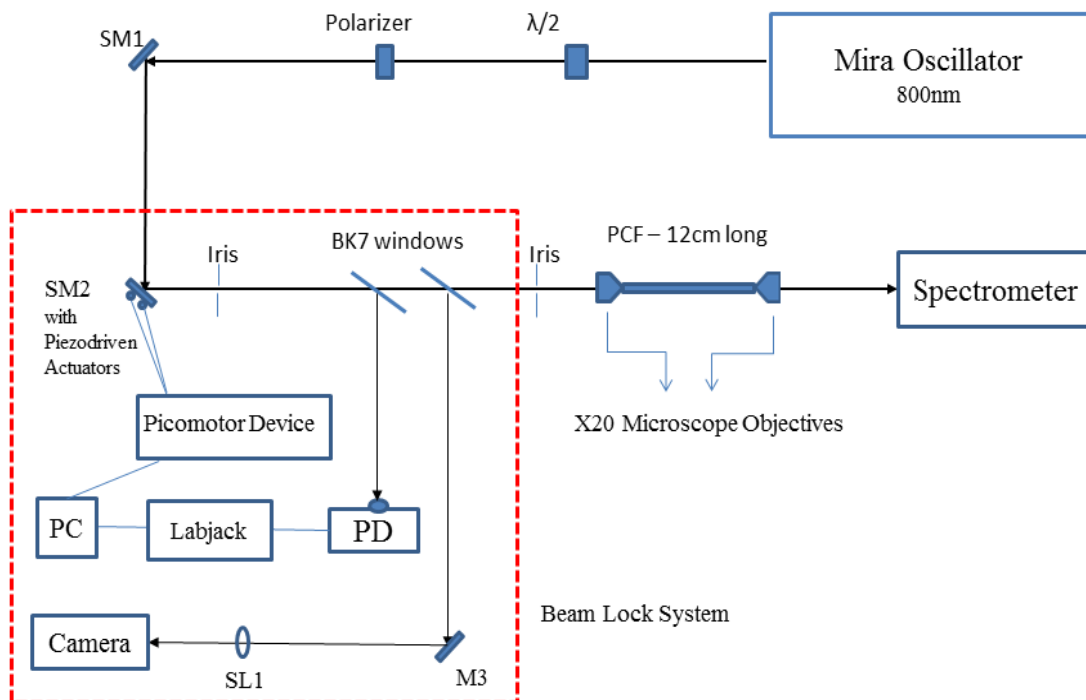


**Figure 14.** Layout of the SC-generating setup with the MIRA Oscillator and the Femtowhite PCF. It also includes; the half-wave plate ( $\lambda/2$ ) and the polarizer for variable input average power, two steering mirrors (SM1, SM2) for leveling the beam, a beam lock system for efficient coupling, fiber's x20 microscope objectives and a spectrometer for intensity distribution measurements.

Two steering mirrors are used to align the beam parallel to the optical axis of the PCF. Before them, a polarizer and a half-wave plate is placed to act as a variable power attenuator for the input pulse. This is a crucial point as aligning with high average powers ( $>50$  mW) could damage the fiber's entrance window. Although the high numerical aperture of the coupling objective focuses the beam very close to the entrance window of the fiber, the auto-steering beam lock system created for the hollow-core fiber was tested here with excellent results.

Purposely misaligning the beam's position relative to the fiber's entrance by manually rotating steering mirror's (SM2) actuators, a larger beam movement was observed at the Photodiode (PD) window. The beam was positioned at the edge of the PD window mostly distributing at the optical area A of the photocell (Figure 12). The program was set to run and very accurately re-positioned the beam at the center of the photodiode and the fiber's core accordingly. Unfortunately, no graph results were obtained during this process but the functionality of the beam lock system was verified. The successful operation of the beam lock system allowed the recording of the output spectra of the PCF since a proper coupling condition was established.

The nonlinear PCF caused spectral broadening of the pulse due to self-phase modulation (Appendix B1) and the light collimated by the output microscope objective was measured with an Avantes spectrometer for intensity distribution spectral measurements of the broadened pulses. Spectra for various input average power were collected by rotating the half-wave plate.

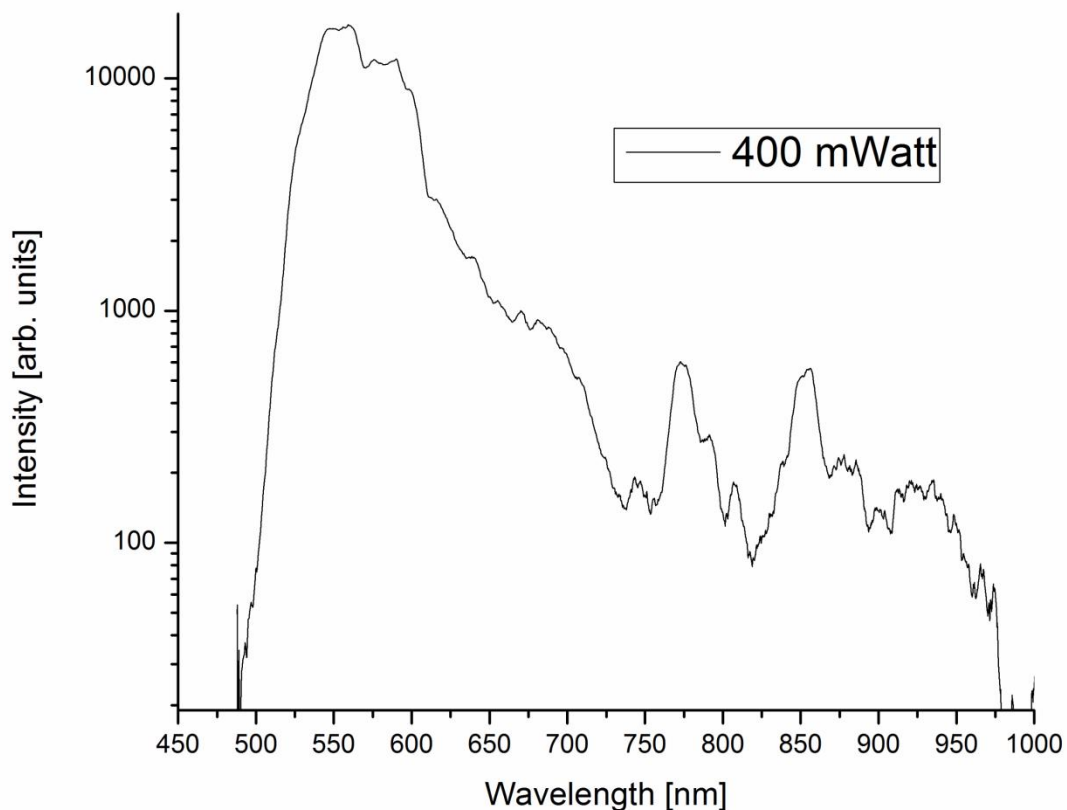


**Figure 15.** Super-continuum spectrum generated in PCF for a 60 fs, 800 nm laser pulse of 400 mWatts average power.

The spectral intensity is normalized in a logarithmic scale to emphasize the magnitude of the generated frequency components. Due to the spectrometer short measurement range, intensity distribution over 1000 nm and below 500 could not be retrieved. The fluctuations of the spectra at these end-values are device errors due to the spectrometer's inability to measure light beyond these points. It is evident that at 400 mWatt power (Figure 15), a large amount of energy transferred on the spectral range of 520-620 nm. The 800 nm component corresponding to the input laser central wavelength contains only a minimal fraction of energy, a phenomenon called pump depletion. This accounts for a successful super-continuum generation where all the input energy originating from the pump wavelengths has distributed almost completely to the newly-generated frequency components. The rate of this procedure relative to the input average power is shown in Figure 16.

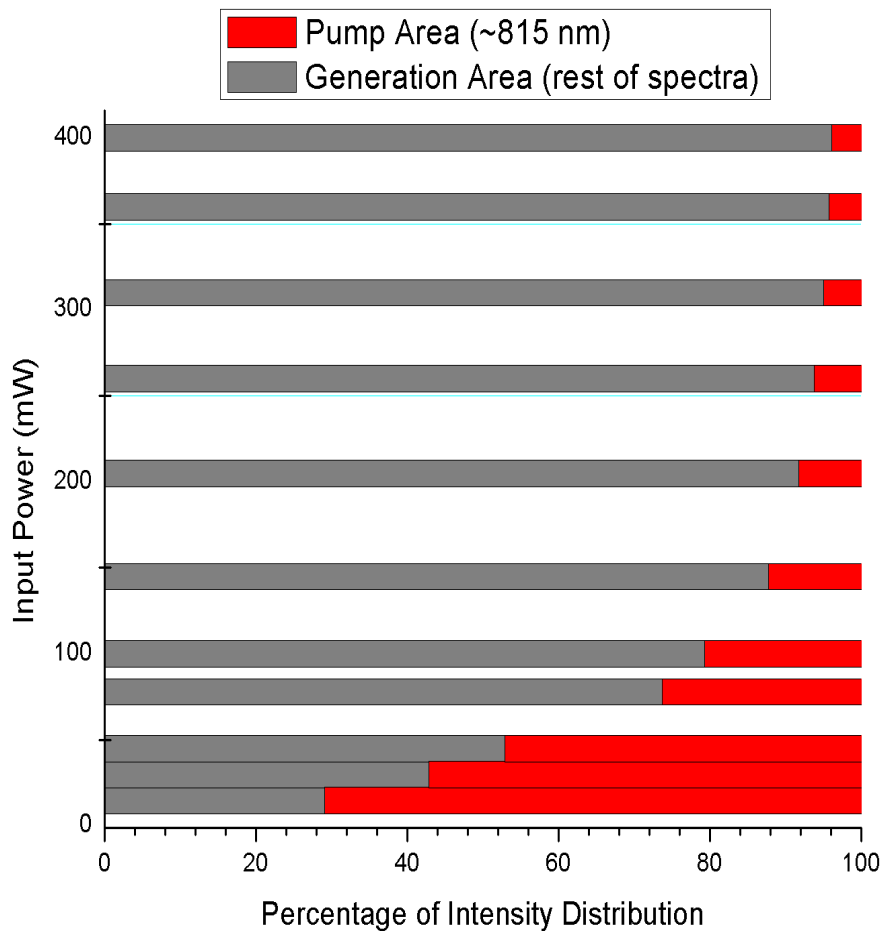


**Figure 16.** Dependence of the pump depletion of the super-continuum spectrum on the power of the input pulse. Red bars show the pump wavelength area and grey bars the rest of the super-continuum spectra

For the lower power values, the energy distribution is mostly confined on the pump wavelength area (>70%) with the spectrum barely being super-continuum as the generation of new wavelength components is minimal. The low input power does not allow strong nonlinear processes to take place inside the fiber; spectral broadening is limited and the output of the fiber is mainly represented by the input wavelength.

However, for higher power coupled in the PCF self-phase modulation broadens the spectrum and the energy distribution for the pump wavelength area drops to 5% for the case of 400 mWatt (highest input power). The efficiency of the spectral broadening can also be derived by the shift noted in the spectral generation maxima for varying input power shown in Figure 17. As the average power increases, the spectrum elongates, more frequency components are generated and the energy is distributed to shorter wavelengths.

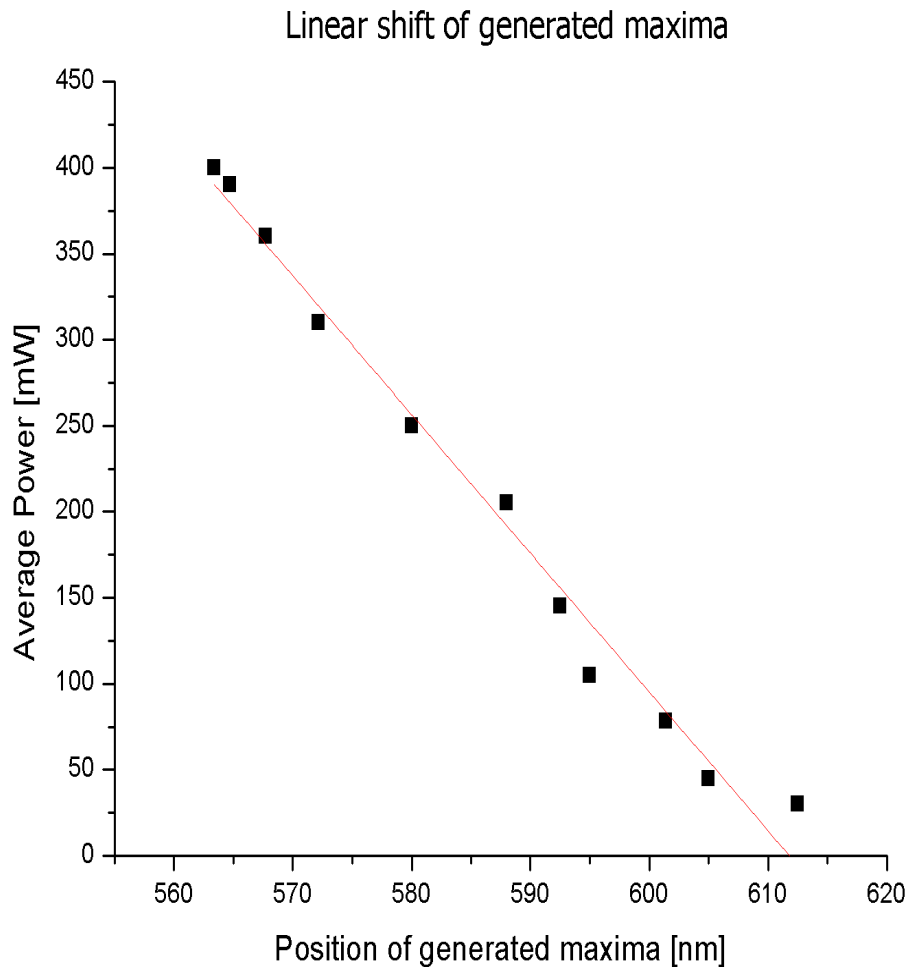


**Figure 17.** Dependence of the maximum of the SC spectrum on the laser input power.

### 2.2.3 Single-Shot FROG

Spectral phase measurement of the hollow core fiber output pulse is of key importance for our 5-fs laser system. The information deduced from this measurement will provide the chromatic dispersion required that a matching set of chirped mirrors must compensate to compress the pulse to 5 fs. For these purposes, a single-shot Second-Harmonic Generation (SHG) FROG device was built and shown in Figure 18. The FROG setup was tested using the fs beam of a MIRA oscillator.

# Single-Shot SHG FROG

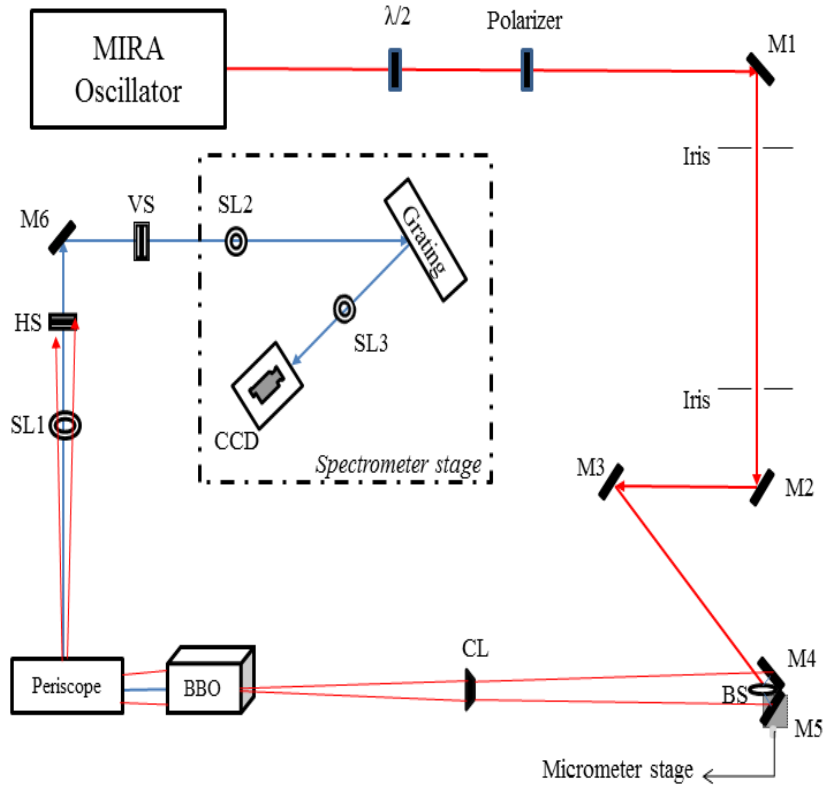


**Figure 18.** Optical layout of our single-shot SHG device. M1-6: mirrors, BS: 50/50 beam-splitter, CL: cylindrical lens, BBO: nonlinear optical crystal, SL1-3: spherical lenses, HS: horizontal slit, VS: vertical slit, CCD: charge-coupled device, Dashed rectangle: contains imaging spectrometer in a Czerny-Turner configuration [38].

For practical purposes, our FROG device was built on a portable plate so its transfer to any experimental setup can be facilitated. The installment of the two Irises seen in the above diagram establishes that once a laser beam is aligned relative to them, a signal at the CCD array is instantly available with no further alignment.

Following the beam propagation, the following optical elements are encountered; a half-wave plate ( $\lambda/2$ ) with a polarizer for variable input power so as small power is supplied during the alignment to prevent damage on the BBO crystal, three steering mirrors (M1, M2, M3) to send the beam to the replica generation stage which includes: a double-mirrored (M4, M5) plane with a 50/50 beam-splitter (BS) in the center that generates the replica of the input pulse. The beam sent in the M5 mirror, which is mounted on a micrometer stage, was manually positioned on the temporal point where the zero delay difference occurs relative to the replica beam driven by M4 so as both beams propagate almost equal optical lengths. Fine tuning to

retrieve the exact point that will satisfy the phase-matching condition for the two beams was performed by the micrometer stage. Once M5's optimal position has been retrieved it stays fixed throughout the experiment. The two beams then are sent to a cylindrical lens of 20 cm focal length (CL) which generates a line focus point and a BBO nonlinear crystal 0.5mm thick was placed on this exact focus point position. The two beams cross the BBO at a certain angle. This crossing angle determines both the temporal resolution and the maximum delay window at the detector. A rough estimation of our crossing angle is around 1.5 degrees.

The interaction of the two beams with the BBO crystal is described in Appendix D. Briefly, there are three beams propagating at the FROG line after the BBO crystal. Two of them are IR beams (and their corresponding co-propagating second harmonics) overlapped in the crystal. The third beam (of frequency  $2\omega_{\text{IR}}$ ) is generated by the spatiotemporal overlap of the two crossing IR beams in the crystal. Due to momentum conservation the later appear in the middle of the two crossing IR beams. In this point it is crucial to eliminate the side beams (converted or not) as they introduce noise and scatter light. The desired beam is the SHG signal generated in the center and with some crystal tilt and/or rotation near perfect phase-matching conditions (momentum conservation) can be satisfied.

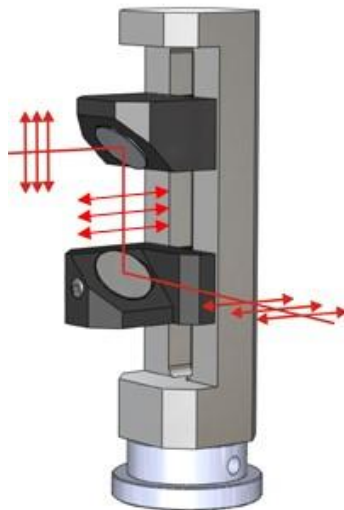


**Figure 19.** Periscope as used in the single-shot FROG device. The red line and arrows show the laser beam path and polarization, respectively.

After the BBO crystal, a periscope was developed for height adjustment and polarization rotation. A sketch of the periscope used is shown in Figure 19. The pulse arriving at the bottom mirror has p-polarization and exits the top mirror with s-polarization. A 4-f configuration with two slits is followed allowing the imaging of the signal at the input of the spectrometer stage. After the crystal, the beams are sent (after passing through the periscope) to a spherical lens (SL1) of 10 cm focal length. A narrow horizontal slit (HS) mounted at the focal plane of the SL1, filters out the unwanted beams as they are now mapped vertically to the table. The slit's opening corresponds to the angular fraction accepted from the interaction on the crystal. A vertical slit (VS) is placed afterwards at a  $2f$  distance from the SL1 and  $f$  relative to

the HS, to be employed as the input slit of the spectrometer stage, thereby concluding the 4-f configuration. The rest of the setup constitutes the imaging spectrometer stage in a Czerny-Turner configuration [38]. A spherical lens of 10 cm focal length (SL2) collimates the harmonic signal to a grating which diffracts the beam. The first order diffracted mode is sent towards a third spherical lens (SL3) of 20 cm focal length which generates the spectrum on the CCD array in f-f configuration. The spectrum is generated on the horizontal axis and the delay on the vertical achieving a single-shot measurement of the SHG signal.

### 2.2.4 FROG Calibration Procedure

A calibration of the FROG trace acquired from the setup in Figure 18 is needed to retrieve pulse's duration and spectral phase. The delay calibration for the single-shot mode of operation is based on theoretical calculations (discussed in Appendix E), requiring a precise knowledge of the crossing angle of the two replica beams on the BBO crystal which is tough to determine at ultimate precision. Hence, a multi-shot auto-correlator was constructed to derive the proper calibration values needed.

## Autocorrelation Setup with Lock-In Amplifier

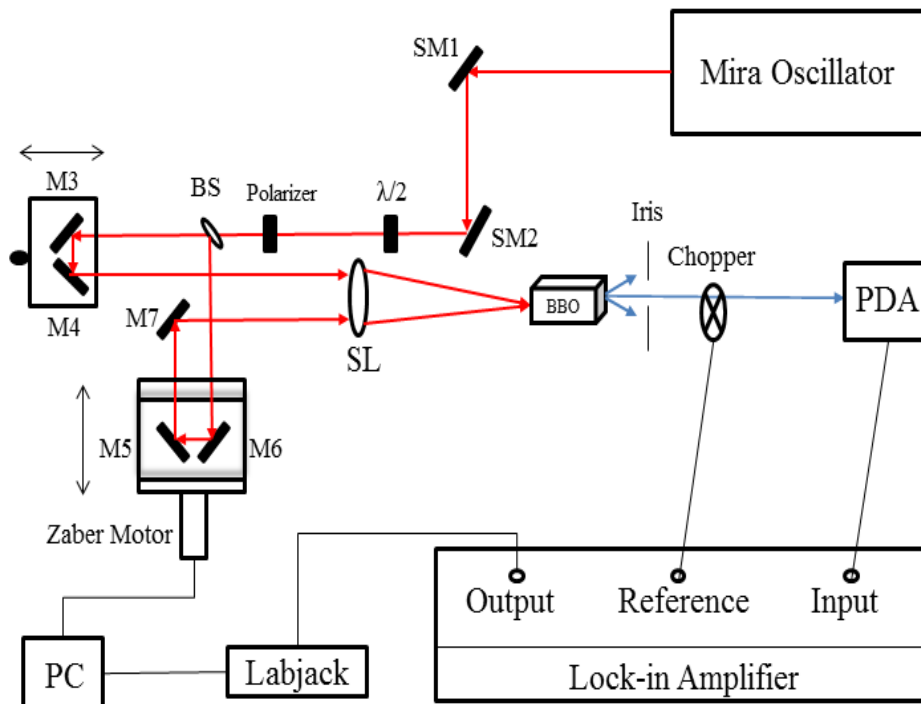


**Figure 20.** Optical layout of the Autocorrelation setup with a lock in amplifier integrated for enhanced sensitivity and noise-free signal measurements. The setup was used for the calibration of the FROG trace. SM1-2: steering mirrors, M3-7: mirrors BS: 50/50 beam-splitter, SL: spherical mirror, BBO: nonlinear optical crystal, PDA: diode array detector, Labjack: data acquisition device, Zaber motor: computer-controlled positioning device, PC: personal computer.

The MIRA fs beam after proper alignment achieved by the two steering mirrors (SM1, SM2) and a pass through the power attenuator system ( $\lambda/2$  and a polarizer) hits a 50/50 beam-splitter which sends one replica to a manual-moving stage (containing mirrors M3, M4) and the other towards a Zaber Motor stage (containing mirrors M5, M6). The Zaber Motor is a computer-controlled positioning device with sub-micron steps. After the consecutive reflections in both stages, another mirror (M7) is used to parallel the two replica beams until a spherical lens of 5 cm focal length (SL). The two arms should be constructed so as light travels equal optical distances for both routes until the replicas meet at the SL. At the SL's focus point, a BBO crystal (the one used for the FROG device) is installed to generate the second harmonic. The multiple-beam output of the BBO encountered at the FROG, appears again and with an almost closed iris all but the SHG autocorrelation signal, diminish. This signal is then sent to an Amplified Photodiode (APD) to measure its intensity as a function of the delay between the two IR replicas.

A Python code instructs the Zaber Motor to perform a small scan around the manually-retrieved zero delay position, locate an improved one and store it. Afterwards, a longer scan with input delay limits and steps, scopes the whole temporal window around the corrected zero delay point. The PDA measures the output intensity for every delay increment, sends it to the Labjack's AIN (Analog Input) port and the corresponding voltage arises for each delay step, recording in this way the AC trace. However, the PDA failed to eliminate the IR noise scattered around the setup despite the iris placement, hence the installment of an analog Lock-in amplifier system was necessary as this device can extract a specific signal from a noisy environment. Integrating it to our layout required inputting the analog signal of the PDA and reference it as the signal of interest with a chopper discriminating it from the scattered IR that also reaches the detector. This discrimination is established due to the chopper inducing a periodicity to the SHG signal.

The SHG signal data are then sent again to the Labjack to reproduce the error-minimizing voltage values for every delay step. The advantage of this setup apart from the noise-free measurements lies on the high sensitivity of the Lock-in amplifier. The 100  $\mu$ Volt scale was used on the experimental process while its sensitivity scales up to 1  $\mu$ Volt. The duration of the pulse is obtained by the AC trace using the

equation  $t_{pulse} = \frac{t_{AC}}{\sqrt{2}}$  where  $t_{AC}$  is the FWHM of the AC trace.

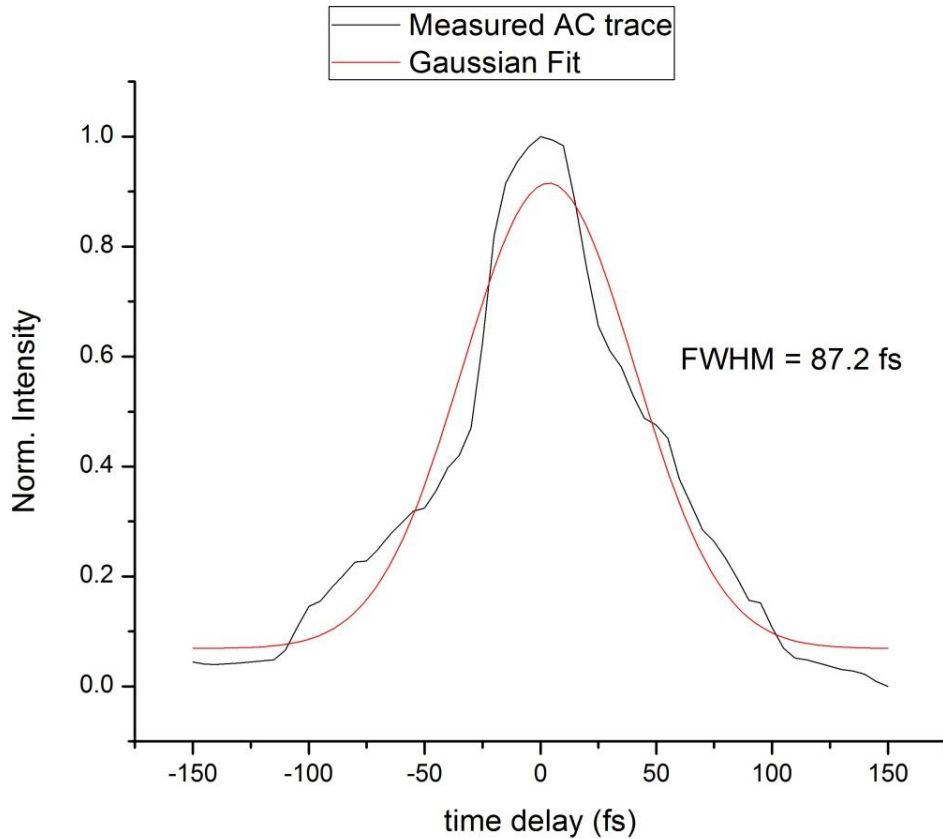


**Figure 21.** AC trace recorded using the fs pulses of MIRA oscillator (black line) and its Gaussian fit (red line).

The autocorrelation signal has a FWHM of 87.2 fs, derived from the Gaussian fit on the experimental data. This corresponds to input laser pulse duration of  $t_{pulse} = 61.6 fs$ . The value of the FWHM of the AC trace (which is 87.2 fs) will be used to define the proper calibration parameters for the FROG trace captured. Sending this value of the FWHM to the FROG algorithm will yield a FROG-AC trace with a FWHM associated with the calibration of the FROG algorithm. Equality between those two fitted FWHM AC values (Figure 22) confirms the validity of FROG's calibration parameters.

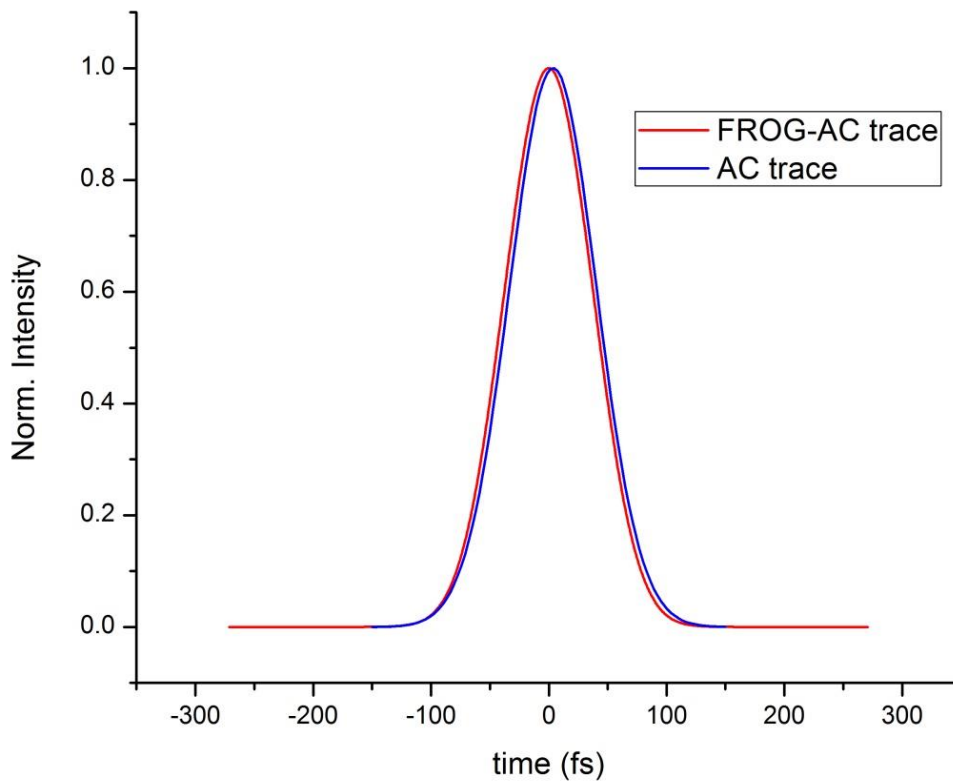


**Figure 22.** Comparison of the FROG-AC (red line) and AC (blue line) traces. Their matching ensures the correct FROG trace calibration parameters.

The FROG trace obtained from the CCD array is captured on a 520x600 pixels format. It is then fed to Femtosoft Technologies software called FROG 3.2.4 version. This software uses the FROG algorithm to retrieve the pulse from the trace with a minimum error rate. An error value less than 0.1% promises a good experimental-retrieval result. Sampling the FROG data, we run the algorithm until the reproduction of a FROG-AC FWHM of 87.2 fs. A temporal window of 275 fs and a wavelength window of 60 nm were the best fitted values of the scan with the algorithm displaying a 0.5% stability error. The FROG error (deviation of raw data with respect to retrieved data) was 0.015%.

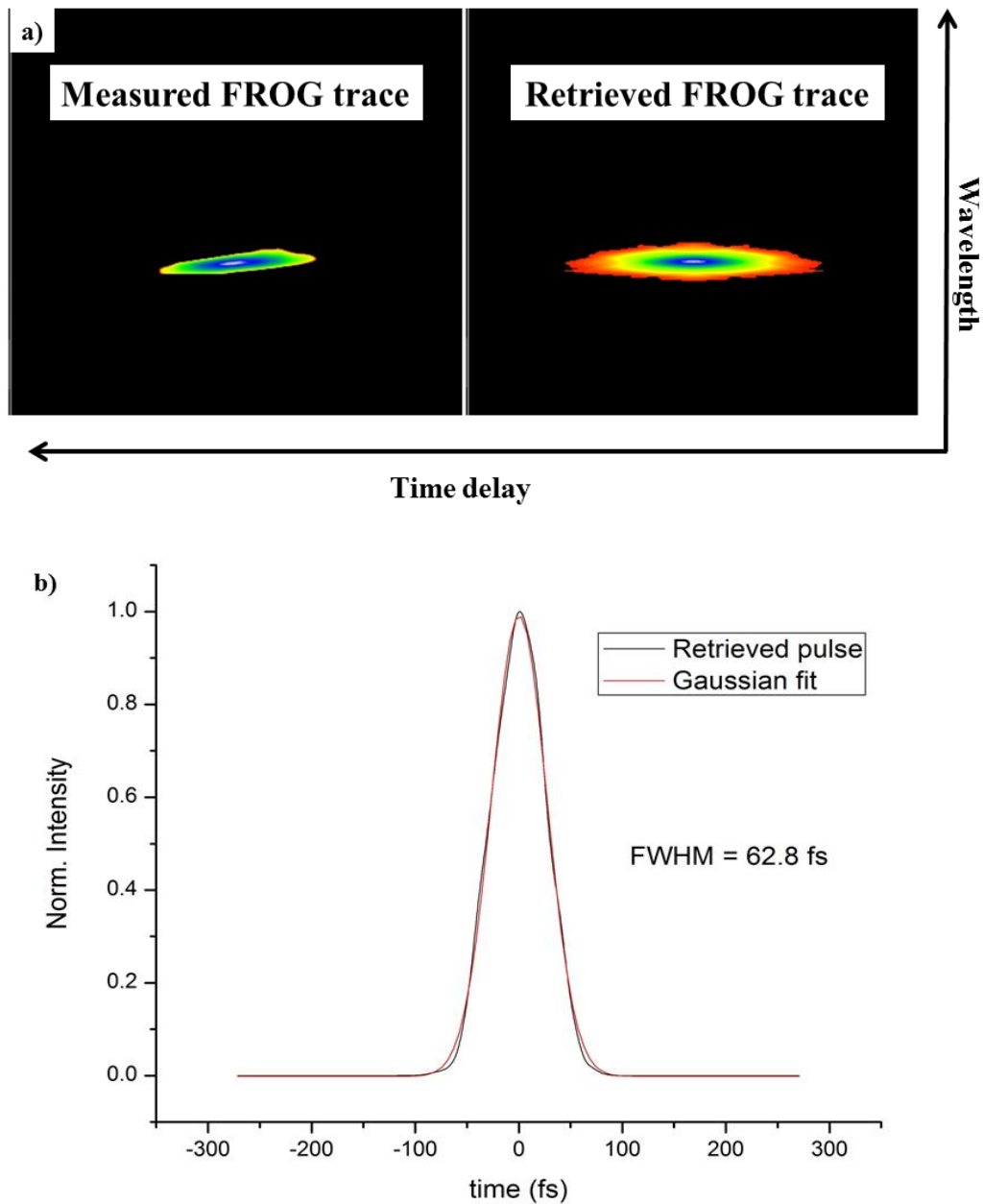


**Figure 23.** a) Measured FROG trace (left column) and retrieved FROG trace (right column), b) Retrieved pulse duration by FROG's algorithm (black line) and Gaussian fit (red line).

The measured and retrieved FROG traces are shown in Figure 23a, while the corresponding pulse duration is shown in Figure 23b. The Gaussian fit on the temporal intensity distribution reveals oscillator's input pulse duration of  $t_{FROG} = 62.9\text{ fs}$  which is found to be larger by 2% compared to the  $t_{AC}$  measured by the AC approach.

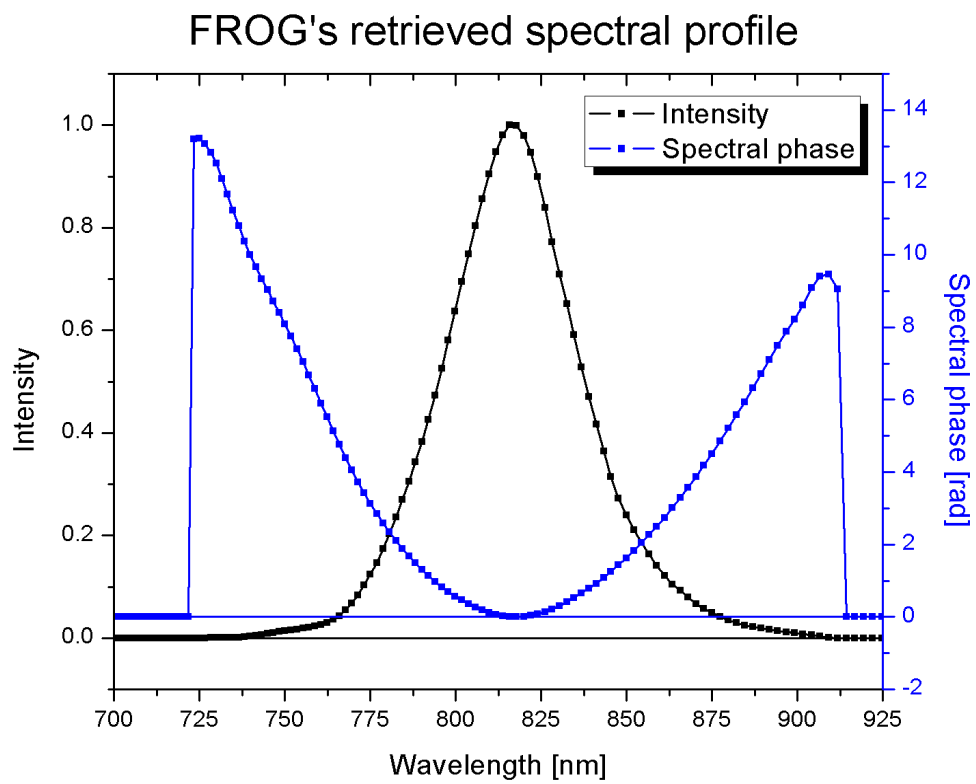
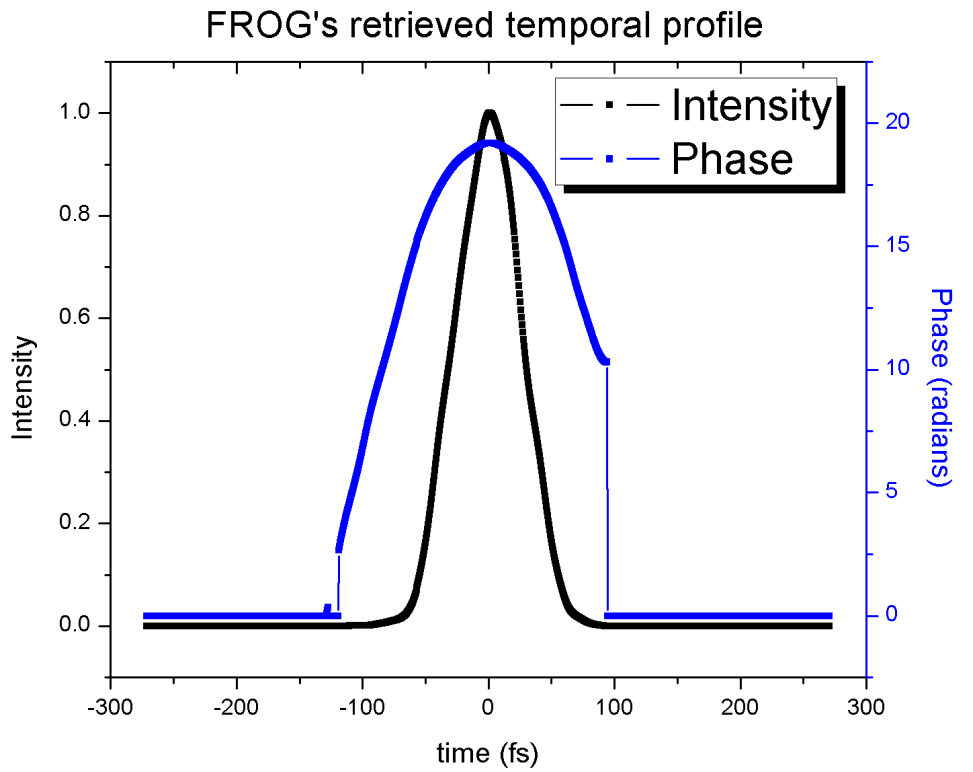


**Figure 24.** Retrieved temporal (up) and spectral (down) profiles of the pulse obtained by FROG's algorithm. Black lines depict the intensity and blue lines the phase distribution, respectively.

The temporal and spectral profiles of the pulse as retrieved by FROG's algorithm are shown in Figure 24 alongside their corresponding phase distribution. The spectral FWHM of the pulse was 42.8 nm with a center wavelength at 815 nm. The phase components retrieved from both temporal and spectral profiles show a positively chirped pulse. This positive GVD entailing the pulse was expected as all optical components induce a positive chirp on the pulse.

The algorithm also provides the Laplacian time-bandwidth product. It describes the factor by which a pulse retrieved abstains from the Fourier transform limit. In our case, the pulse broadening was found to be 3 times larger compared to the FTL case which corresponds to pulse duration of 20 fs. This broadening is attributed to the positive chirp introduced to the pulse by the used optics.

### **3. Conclusion**

The 5-fs beam line is currently under development in Attosecond Science and Technology laboratory in FORTH-IESL. In this thesis, a beam stabilization system for efficient fiber coupling and a FROG device for pulse characterization are presented as they have been built and tested. These segments will be installed integrally in our 5-fs setup. The output IR pulses will be eventually used for the generation of attosecond XUV radiation in various ultrafast dynamics experiments like High-Harmonic Generation (HHG) in gases.

## 4. Appendixes

### Appendix A. Photonic Crystal Fibers

A major step for efficient SC generation was provided by the advancements in optical fiber production technique. SC generation experiments with fibers had already been started since the 70's. However, the production of the first PCF by Knight et al [5] in 1996, overcame limitations imposed by traditional optical fibers. The photonic crystal design is arranged in a scheme of tiny and closely spaced air holes that delivers its properties. The core which confines the light is either fused silica-based or air-based, dividing the PCFs to two main categories, *solid core PCF* (also known as index-guiding PCFs) and *hollow core fibers* (HCFs) respectively (also known as band-gap fibers).

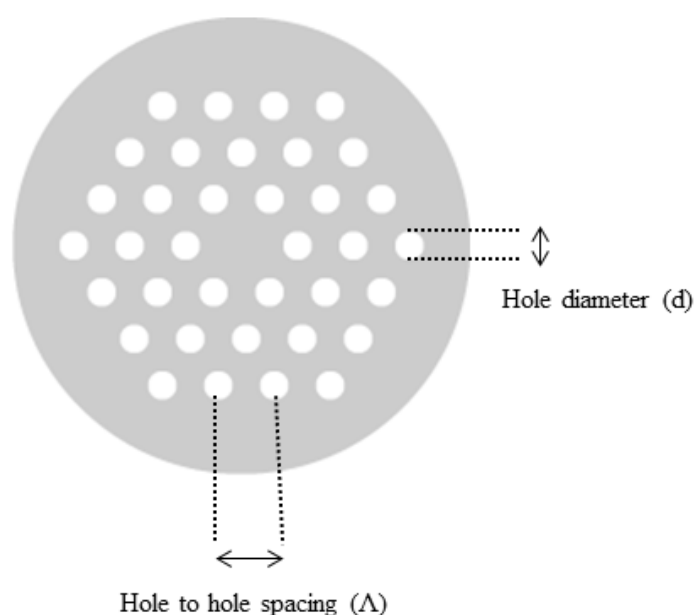


**Figure A1.** Solid core photonic crystal fiber cross-section. It depicts a triangular pattern of air holes with the central hole missing. Lattice parameters: hole to hole spacing ( $\Lambda$ ) and hole diameter ( $d$ ).

Guidance in solid core PCFs occurs similarly to the total reflection regime already known from conventional optical fibers. The refractive index of the core material is larger than the refractive index of the air hole lattice so guidance occurs via total internal reflection. In hollow core fibers the light is confined by a photonic band-gap created by the photonic crystal. Light guidance in hollow core fibers has proven popular due to limited distortion effects inducted by the air core. PCFs, in general, exhibit the advantages of the large core-cladding refractive index contrast (silica with air) which provides higher confinement and greater nonlinearity. Also, the capability of engineering the dispersion waveguide is provided, by shifting the zero dispersion wavelength (ZDW) into the visible. Apart from these, PCFs offer endlessly single mode propagation even for large mode area fibers (over 100  $\mu\text{m}$  core diameter). The ZDW can be configured by adjusting the hole lattice parameters surrounding the core. The dimensions of the PC cladding are described by the hole to hole spacing ( $\Lambda$ ), and the hole diameter ( $d$ ) (see Figure A1). In silica, common material for solid core PCFs, the intrinsic ZDW is around 1.3  $\mu\text{m}$ . Suitable designs can deliver it at shorter wavelengths close to the laser pump wavelength with ultra-broadband spectra emitted.

In light propagation through fibers, the effective refractive index experienced by different wavelength components is affected by the geometry of the waveguide since the modes supported by the waveguide, are wavelength-dependent. As a result, shorter wavelength components get more confined to the core, a phenomenon called *waveguide dispersion*. Together with the *material dispersion* induced by incident light pulses causing temporal spreading of the pulse, the peak power of the pulse and the nonlinearity decrease in magnitude. The total dispersion can be described by a Taylor series approximation of the propagation constant  $\beta(\omega)$  about the pulse's central angular frequency ( $\omega_0$ ) as:

$$\beta(\omega) = \beta_0 + \beta_1(\omega - \omega_0) + \frac{\beta_2}{2}(\omega - \omega_0)^2 + \dots \quad (\text{A1})$$

Where  $\beta_0$  is the inverse of the phase velocity ( $u_p$ ) of a wave at a single frequency or else the effective refractive index of the propagating mode,  $\beta_1$  is the inverse of group velocity ( $u_g$ ) which is the envelope's velocity of propagation. Practically,  $\beta_1$  describes the waveguide dispersion and  $\beta_2$  represents the *Group Velocity Dispersion (GVD)* given by:

$$\text{GVD} = \frac{d^2 \beta}{d\omega^2} \quad (\text{A2})$$

GVD is usually measured in  $[\text{s}^2/\text{m}]$ . Concerning higher order dispersion terms, it is important to recall the zero dispersion wavelength (ZDW). ZDW is defined as the spectral point where the fiber's dispersion parameter  $D$  is cancelled. Laser pulses that insert the fiber at the ZDW, undergo the minimum spreading in time caused by dispersion and only higher order dispersion terms become effective. Ultimately, it is a modification of the group-velocity dispersion (GVD) of the fiber. GVD arises from the frequency dependence of the refractive index and causes temporal spreading to the pulse and the distribution of distinct frequency components at different times. The two regimes are; *normal GVD* ( $\beta_2 > 0$ ) meaning that low frequencies components have a higher group velocity than higher frequency components (negative chirp) and *anomalous GVD* ( $\beta_2 < 0$ ), where higher frequency components are on the trailing edge of the pulse (positive chirp). As a result, ZDW engineering allows both normal and anomalous dispersion impending effects to be explored.

Chirping caused by dispersion deprives the pulse from its transform limited temporal profile and induces non-flat spectral phase. From the *time bandwidth product* (TBP) of the pulse, it is trivial to extract the presence and magnitude of chirp on the pulse. For a transform limited Gaussian pulse, TBP equals 0.441 whilst for a hyperbolic secant ( $\text{sech}^2$ ) pulse 0.315 [6]. Other parameters commonly used in dispersion phenomena are the *dispersion coefficient* ( $D$ ) and the dispersion length given respectively by:

$$D = \frac{d\beta_1}{d\lambda} = -\left(\frac{2\pi c}{\lambda^2}\right)\beta_2 = -\frac{\lambda}{c} \frac{d^2 n}{d\lambda^2} \quad (\text{A3})$$

$$L_D = \frac{T_0^2}{|\beta_2|} \quad (\text{A4})$$

where  $T_0$  is the half width at 1/e intensity point of the pulse. The *dispersion length*  $L_D$  defines the length scale over which dispersion is significant during pulse propagation. It is a rough approximation of the length required due to dispersion for a transform limited pulse to double its temporal width.  $T_0$  relates to the full-width at half maximum (FWHM) of a Gaussian pulse through:

$$T_{FWHM} = \tau = 2\sqrt{\ln 2}T_0 = 1.665T_0 \rightarrow \text{Gaussian} \quad (\text{A5})$$

## Appendix B. Nonlinear Dynamics

A pivotal step to enforce supercontinuum generation has been the progress in mode-locked femtosecond lasers. Firstly introduced by Rolland et al. in the 1980's [7], these revolutionary sources blossomed in the 1990's. In their pulsed mode of operation they can deliver peak powers in the order of kilowatts with electric field amplitude reaching values in the order of  $10^{11}$  V/m coupling intensities to the interatomic regime [8]. Since pulse's peak power is inversely proportional to the pulse duration, ultra-short pulses with large spectral bandwidth are produced. Reaching these intensity scales provided the chance to study in detail the main nonlinear effects taking place in SC generation during the pulse propagation in the fiber. Starting from the linear optical regime, the *induced polarization* in a dielectric medium is given by:

$$\vec{P} = \epsilon_0 \chi \vec{E} \quad (\text{A6})$$

Where  $\epsilon_0$  is the *permittivity of free space*,  $\chi$  is the *susceptibility parameter* and  $\vec{E}$  is the electric field. Increasing the electric field amplitude to values above the atomic threshold, the nonlinear terms should also be taken into account by expanding the induced polarization as:

$$\vec{P} = \epsilon_0 \left( \chi^{(1)} \vec{E} + \chi^{(2)} \vec{E}^2 + \chi^{(3)} \vec{E}^3 + \dots \right) \quad (\text{A7})$$

Where  $\chi^{(n)}$  is the nth order susceptibility,  $\chi^{(1)}$  the linear term,  $\chi^{(2)}$  the second order susceptibility which is related to nonlinear effects such as *second harmonic generation (SHG)*. However, this term and all the even ones in return vanish for structures with inversion symmetry in the dipole approximation (i.e. silica glass). As a result, most of the nonlinear effects presented in silica fibers originate from the third order susceptibility (Kerr effect, Raman scattering etc.) as the higher order terms require even stronger fields which are undesirable as they lead to ionization and eventual material destruction.

The *Kerr effect* in general is the intensity dependence of refractive index. It has a quadratic dependence on the applied external electric field or the induced electric field of a laser pulse propagating through a medium (Optical Kerr Effect). The total refractive index concludes to:

$$n = n_0 + \frac{3\chi^{(3)}}{8n_0} |E_A|^2 = n_0 + n_2 I \quad (\text{A8})$$

Practically, this means that the laser pulse can alternate the refractive index properties of a medium while propagating on it. Kerr effect gives rise to many nonlinear effects such as Self-Phase Modulation (SPM), Cross-Phase Modulation (XPM), self-steepening, modulation instability (MI) and four-wave mixing(FWM).

## Appendix B1. Self-Phase Modulation (SPM)

One of the most critical effects of the Kerr nonlinearity is *self-phase modulation (SPM)*. Due to the modification of the refractive index in the presence of an intense laser pulse, a temporal phase shift is also imposed, apart from the linear phase shift caused by propagation, leading to differentiations in the frequency spectrum of the pulse. Unlike dispersion, SPM does not induce temporal broadening to the pulse, but it broadens the spectrum symmetrically [9]. This spectral broadening is the main mechanism behind SC generation for femtosecond pulses propagating in nonlinear fibers. An insight of SPM physical process can be deduced from the time-dependence acquired by the refractive index of the medium from the propagating intense pulse. The refractive index will copy the temporal shape of the intensity and by affecting the light wavelength, will eventually cause a shift in the instantaneous phase of the pulse defined as:

$$\varphi(t)|_{tot} = \omega_0 t - \left( \frac{2\pi}{\lambda_0} \right) n(I) z \quad (\text{A9})$$

With  $\omega_0$  and  $\lambda_0$  representing the vacuum frequency and wavelength of the pulse and  $z$  being the effective propagation length of the pulse in the material. Respectively, the instantaneous frequency shifts as:

$$\omega(t) = \frac{d\varphi(t)}{dt} = \omega_0 - \frac{2\pi}{\lambda_0} n_2 \frac{dI(t)}{dt} z \quad (\text{A10})$$

The frequency shift is presented below with the leading edge of the pulse moving towards lower frequencies (longer wavelengths generated) and the trailing edge towards higher frequencies (shorter wavelengths generated) with the center of the pulse and the tails remaining constant.

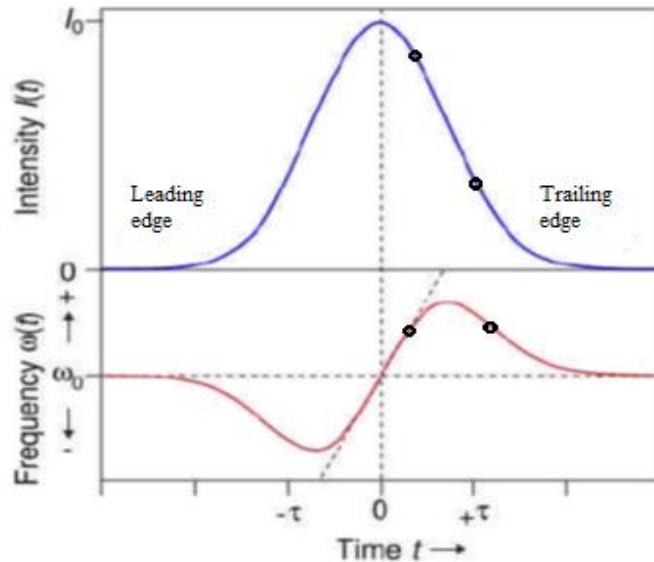


**Figure A2.** Self-frequency shift induced by Self-phase Modulation.

The frequency shift satisfies a linear equation with  $\alpha$  being its slope corresponding to the linear chirp coefficient. This coefficient is given by:

$$\alpha = \left. \frac{d\omega}{dt} \right|_0 = \frac{4\pi n_2 z I_0}{\lambda_0 \tau^2} \quad (\text{A11})$$

From Figure A2 we can distinguish the chirp induced for  $t = \pm t/2$  which is needed for pulse compression (positive slope and chirp), the opposite one induced towards the wings of the pulse which leads to temporal broadening and the bending points in-between which represent non-linear chirping. The dots represent two waves at different temporal positions experiencing the same frequency shift (same chirp). Their phase difference determines the spectral intensity at that frequency depending on their constructive or destructive interference.

### Appendix B1.1 Self-Phase Modulation including normal dispersion

Ultra-short pulses require a different approach than the one described above since material dispersion cannot be neglected during SPM as these two mechanisms affect each other. Normal dispersion alters pulse properties of the SPM broadened pulse and rapidly reinforces its spectrum elongation with propagation. A flat topped intensity profile and a temporally broadened linearly chirped pulse are the results of dispersion embodiment as shown in Figure A3. The latter enables a larger fraction of the input energy to append to the compressed pulse.

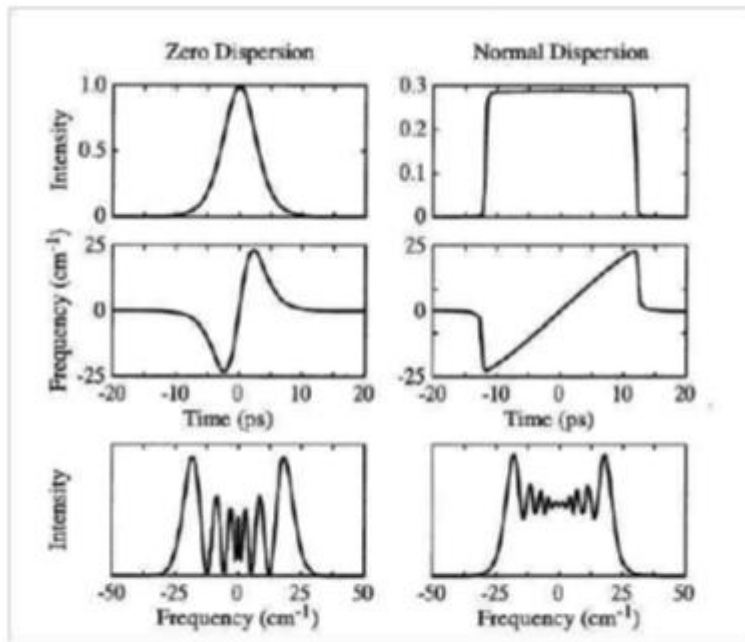


**Figure A3.** Pulse undergoing SPM without dispersion (left column) and with dispersion (right). From ref. [10]

SPM and normal dispersion produce a pulse broadening 3 times longer than the one expected for dispersion-only appliance, independent of the input laser and

fiber parameters. To secure the maximal energy in the eventual compression scheme, an optimal fiber length has to be chosen around [11]:

$$z_{opt} \approx 2.5\sqrt{L_D L_{NL}} \quad (A12)$$

The dispersion length  $L_D$  is defined in Equation 4 and the nonlinear length  $L_{NL}$  as the propagation length in which nonlinear effects take place and is given by:

$$L_{NL} = \frac{1}{\gamma P_0} \quad (A13)$$

Nonlinear length has units of  $[W^{-1}/m]$  and depicts a figure of merit for fibers with  $P_0$  the pulse peak power and  $\gamma$  the nonlinear parameter of the fiber given by,

$$\gamma = \frac{n_2 \omega_0}{c A_{eff}} = \frac{2\pi n_2}{\lambda_0 A_{eff}} \quad (A14)$$

With  $A_{eff}$  representing the effective area of the mode. Returning to Equation A12, the optimal fiber length is greatly influenced both by fiber's parameter and pulse's properties.

### Appendix B1.2 SPM and anomalous dispersion

As discussed above, SPM and normal dispersion interfere constructively for a rapid spectral broadening. However, when pumping in the anomalous dispersion regime, the SPM-induced chirp and dispersion can be balanced out, leading to the generation of optical solitons waves which propagate without distortion for appreciable distances [12]. The resulting spectrum for soliton-related dynamics is a broadband continuum with the drawbacks of the complicated pulse structure and the limited amount of energy that can be coupled into the fiber. Solitons are very sensitive to perturbations and laser noise producing a spectrum which fluctuates in intensity and phase pulse to pulse. The technical engineering required to relocate the ZDW to shorter wavelengths in order to pump on the anomalous dispersion regime sets a limitation to the core diameter ( $< 3 \mu m$ ), so the coupled energy into the fiber scales accordingly (maximally few nJs). This attributes result to a spectrum requiring a complicated experimental compression [3].

### Appendix B2. Self-Steepening

*Self-steepening* is a process stemming from the intensity dependence of the group index. The peak of the pulse exhibits higher group index than the rest of the pulse and propagates with a lower velocity. As a result, defining an intensity gradient between the leading and the trailing edge, an increase is spotted in the trailing edge and a decrease in the leading. The spectrum generated by SPM undergoes asymmetries and an increased broadening on the short wavelength side, when a strong self-steepening effect is present. Self – steepening is an important mechanism when pumping with ultra-short (femtosecond) pulses.

### Appendix B3. Self-focusing

Self-focusing is another process of the third order nonlinearity regime originated from the Kerr effect. It describes the increased refractive index that the inner part of the beam experiences compared to the outer due to the spatial intensity distribution of the beam itself. The created refractive index gradient acts as a focusing lens, leading to a beam size gradually reduced with propagation. The smaller spot size contains the intensity distribution of the incident larger spot affecting afresh the

refractive index of the medium and the process cycles to more intense self-focusing effects until a collapse of the beam on itself. Self-focusing occurs if the radiation power is greater than the critical power.

$$P_{CR} = \alpha \frac{\lambda^2}{4\pi n_0 n_2} \quad (\text{A15})$$

Where  $\alpha$  is a constant depending on the initial spatial distribution of the beam. For a Gaussian beam it is estimated around 1.89. For silica and 800nm pump wavelength the critical power is around 2.8 MW. The critical power does not depend on the incident beam size. In optical fibers, self-focusing reduces the effective mode area which approaches zero at the point at the point of critical power. For pulsed laser systems, the critical power is determined by the peak power and not by the average power.

### Appendix C. Super-Continuum Generation

As already described, Super-Continuum generation is defined as the spectral broadening of a pump pulse due to the nonlinear effects shown above. The output forms a continuous spectra with wavelength components spanning from the deep XUV to above IR. After its first observation in bulk material, SC was generated in conventional fibers by Lin and Stolen [20] with enhanced spatial profile and improved efficiency. Their output contained 200 THz bandwidth with normal GVD pumping and it was attributed to Raman Scattering and SPM. It was the advent of PCF that greatly improved SC generation. The capability of dispersion engineering which unfolds the anomalous dispersion regime and the tight confinement which increased efficiency were revolutionary steps towards a broader spectrum. The soliton propagation regime was first observed by Mollenhauer in 1973 in a wide spectrum where higher order solitons were spawned.

Alfaro and Shapiro white light (first introduced) spanned through the entire visible range which was a spectra ten times wider than anything previously reported. The first octave spanning SC was generated in 2000 with PCF using nanoJoule energy pulses from a Titanium: Sapphire laser [21]. A 550 THz bandwidth with 100 fs input pulses was generated. Comparable spectral broadening was achieved in bulk material with the expense of mJoule sources and a less uniform spatial profile as filamentation effects are presented in bulk experiments.

Super-continuum applications include spectroscopic studies where the broad spectrum is used for simultaneous excitations of multiple compounds with high sensitivity [23]. Biomedical imaging is a science field where appliance of SC can be met, especially in Optical Coherence Tomography where it is used for finding eye defects [24]. Other applications include dynamic surface characterization by white light interferometry [25], optical frequency metrology [26], broad-band optical communication systems [27], tunable lasers [28] and of course pulse compression which is the eventual purpose of this thesis.

A special note should be given on frequency metrology since it became possible to measure and control the absolute position of the frequency comb, consisting of the modes of a femtosecond laser pulse train with the SC spectra, using an interferometric technique [29]. Since stabilizing the frequency comb is equivalent to carrier-envelope phase (CEP) stabilization, ultrafast optical processes such as generation of attosecond pulses though high harmonic generation and above-threshold ionization can be explored [3].

## Appendix D. Second-Harmonic Generation

With the use of a nonlinear crystal (i.e. BBO) it is possible to generate a frequency doubled wave of the input frequency wave inside the crystal. The physical mechanism behind this process lies on the second order nonlinearity introduced by the crystal to the pump IR beam ( $\omega_{\text{IR}}$ ) that generates a nonlinear polarization wave of  $2\omega_{\text{IR}}$ . Energy and momentum conservation conditions govern the process. Energy-wise, two photons of the fundamental frequency are annihilated and one at the second harmonic is generated. Thus, the system's overall energy is conserved. Momentum conservation also known as phase-matching condition, demands that the two wave-vectors of the annihilated photons add up to the wave-vector of the second-harmonic photon. Interference of the two input IR pulses in the crystal yields second harmonic signals at each side of the crossing IR beams and by eliminating the wave-vectors mismatch, complete spatiotemporal overlapping can be achieved delivering a second harmonic signal at the center of the two beams. As depicted in Figure A4, the two pulses have a fixed angle between them, determined by the maximum phase-matching achieved and this angle is responsible for the resolution of the recordable pulse duration. Inside the crystal, the crossed wavefronts induce second-order processes and transform the temporal distribution into spatial intensity distribution of the signal in the x-axis

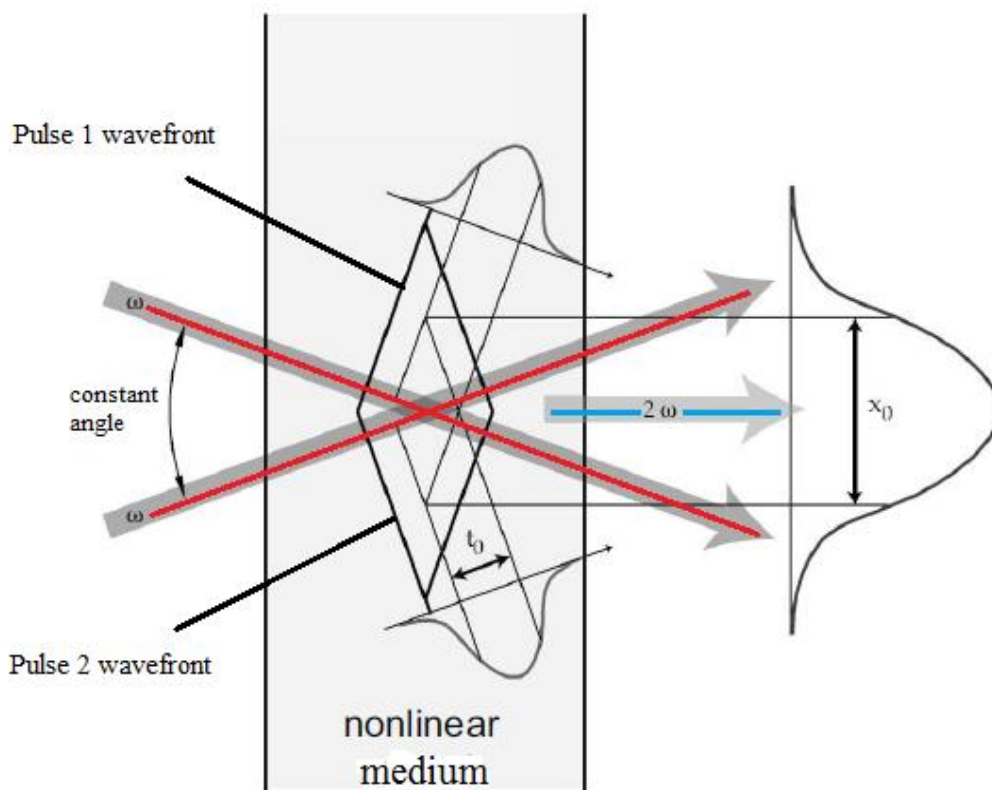


**Figure A4.** Second-Harmonic Generation process. Two IR pulse wave-front crossing in a nonlinear medium at constant angle require perfect wave-vector overlapping to produce a  $2\omega$  signal at the centre of the medium. Temporal properties of the pulse ( $t_0$ ) are projected on the x-axis of the crystal.

## Appendix E. FROG Calibration

To correctly define a FROG trace captured in a SHG experiment, a calibration process is required for both the time and the wavelength axis of the trace recorded in the CCD camera after the second harmonic generation. Time calibration in single-shot FROG requires a theoretical approach as the signal contains a delay axis which is mapped on a lattice of pixels. The delay time between adjacent pixels is calculated as follows:

The spatial length ( $\alpha$ ) of a beam in a medium is:

$$\alpha = \frac{c_0}{n_{medium}} \tau_{FWHM} \quad (A16)$$

Due to the cylindrical lens the pulse propagation can be analyzed two-dimensionally. The length of the *interaction region* ( $z$ ) inside the medium expressed relative to the *interpulse angle* ( $\theta$ ) sums to:

$$z(\theta) = L \tan\left(\frac{\theta}{2}\right) + \frac{2\alpha}{\tan(\theta)} \approx \frac{2\alpha}{\tan(\theta)} = \frac{2c_0}{n_{medium} \tan(\theta)} \tau_{FWHM} \quad (A17)$$

The delay dispersion is given by:

$$T = \frac{2\tau_{FWHM}}{z(\theta)} = \frac{n_{medium} \tan(\theta)}{c_0} \quad (A18)$$

The delay dispersion measured in  $\frac{time}{length}$  can easily conclude to  $\frac{time}{pixel}$  by knowing the detector's unit cell size which represents the pixel spacing. Wavelength spacing on the other hand can be obtained with a calibration lamp placed in front of the input slit of the spectrometer (grating and lens). The fixed distance of the CCD and the spectrometer is a prerequisite. The diffracting frequencies emitted in the wavelength axis of the CCD have known emission lines. As a result the central wavelength (800 nm) can be centered in the middle of the wavelength axis and with a second emission line an estimation of the frequency window can be made.

Another method for time and frequency spacing calibrations of single-shot FROG is a multi-shot SHG autocorrelation setup as done in the present work where we used the AC trace as a guide to correctly define FROG's trace calibration values.

## 5. Acknowledgements

First of all, I would like to show my gratitude to my supervisors; Professor Dimitrios Charalambidis and Doctor Paraskevas Tzallas for introducing me to the physics of Attosecond science. Their guidance throughout this work was of great importance and their entrusting me with this project will always be appreciated. Special thanks should be attributed to researcher David Gray who was always there for me and together we carried out the whole experimental and analysis project. His knowledge and influence provided the basis of my work and for that I am grateful. Last but not least, Nikos Papadakis provided all the technical assistance needed and helped me on many levels throughout this work.

## 6. References

- [1] Thomas Ganz, "Supercontinuum Generation by chirped pulse compression for Ultrafast Spectroscopy and broadband near-field microscopy", Dissertation an der Fakultat für Physik, München 2011.
- [2] R. Alfaro and S. Shapiro. "Emission in the region 4000 to 7000 angstrom via four-photon coupling in glass" *Phys. Rev. Lett.*, vol. 24, pp. 584-587, 1970.
- [3] J. M. Dudley, G. Genty and S. Coen, "Supercontinuum generation in photonic crystal fiber", *Rev. Mod. Phys.*, vol. 78, pp. 1135-1184, 2006
- [4] R. Szipocs et al., "Chirped multilayer coating for broad-band dispersion control in femtosecond lasers", *Opt. Lett.* 19 (3), 201 (1994)
- [5] J. C. Knight, T. A. Birks, P. S. J. Russell and D. M. Atkin, "All-silica single-mode optical fiber with photonic crystal cladding", *Opt Lett.*, vol.21, no.19, pp.1547-1549, 1996
- [6] K. L. Sala, G. A. Kenney-Wallace and G. E. Hall. CW Autocorrelation Measurements of Picosecond Laser Pulses. *IEEE Journal of Quantum Electronics*, 16 (9): 990-996, 1980
- [7] C. Rolland and P. B. Corkum, "Generation of 130-fsec midinfrared pulses", *JOSA B*, vol.3 no.12, pp.1625-1629, 1986
- [8] Mikko Narhi, "Towards complete characterization of supercontinuum coherence", Master of Science thesis, 2013
- [9] A. Weiner, Ultrafast optics. John Wiley and Sons, 2009.
- [10] F. Keilmann et al., DE102005050151 (2006)
- [11] W. J. Tomlison, R. H. Stolen and C.V. Shank, Compression of optical pulses chirped by self-phase modulation in fibers. *J. Opt. Soc. Am. B*, 1(2):139-149, 1984
- [12] A. Hasegawa and F. Tappert, "Transmission of stationary nonlinear optical pulses in dispersive dielectric fibers. i. anomalous dispersion" *Applied Physics Letters*, vol. 23, no.3, pp.142-144, 1973.
- [13] A. Hasegawa and F. Tappert, "Transmission of stationary nonlinear optical pulses in dispersive dielectric fibers. i. anomalous dispersion" *Applied Physics Letters*, vol. 23, no.3, pp.142-144, 1973.
- [14] F. M. Mitschke and L. F. Mollenauer, "Discovery of the soliton self-frequency shift". *Opt. Lett.*, vol. 11, no.10 pp. 659-661, 1986
- [15] N. Akhmediev and M. Karlsson, "Cherenkov radiation emitted by solitons in optical fibers" *Phys. Rev. A*, vol 51, pp.2602-2607, 1995
- [16] M. Miyagi and S. Kawakami, "Design theory of dielectric-coated circular metallic waveguides for infrared transmission," *J. Lightwave Technol.* LT-2, 116-126 (1984).
- [17] R. Boyd, *Nonlinear Optics*, 3<sup>rd</sup> edition. Academic Press, 2008
- [18] S. Bohman et al. "Generation of 5 fs, 0.5 TW pulses focusable to relativistic intensities at 1KHz", *Optics Express* 10685, Vol. 16, No. 14 (2008)
- [19] D. Skryabin and A. Yulin, "Theory of generation of new frequencies by mixing of solitons and dispersive waves in optical fibers" *Phys. Rev. E*, vol.72, pp. 1547-1549, 2005
- [20] C. Lin and R. H. Stolen "New nanosecond continuum for excited-state spectroscopy". *Applied Physics Letters*, 28(4): 216, 1976
- [21] J. K. Ranka, R. S. Windeler and A. J. Stenz, Visible continuum generation in air silica microstructure optical fibers with anomalous dispersion at 800 nm. *Optics Letters* 25(1):25-27, 2000
- [22] D. Mogilevtsev, T. A. Birks and P. St. J. Russell, "Group-velocity dispersion in photonic crystal fibers", *Opt Lett.* 23, 1662-1664, 1998
- [23] T. K. Laurila, S. Kiwanuka, J. H. Frank and C. F. Kaminski, "Broadband cavity-enhanced spectroscopy using supercontinuum radiation" in *Lasers. Sources and Related Photonic Devices*. Optical Society of America, 2012, p. LT5B.4

- [24]A. F. Fercher, K. Mengedoht and W. Werner, "Eye-length measurement by interferometry with partially coherent light", *Opt. Lett.*, vol. 13 no. 3, pp. 186-188, 1988.
- [25]P. Ryczkowski, A. Nolvi, I. Kassamakov, G. Genty and E. Haeggstrom, "High-speed stroboscopic imaging with frequency doubled supercontinuum", *Opt. Lett.*, vol. 38, no. 5 pp. 658-660, 2013.
- [26]R. Wu, V. Torres-Company, D. E. Leaird and A. M. Weiner, "Supercontinuum-based 10-ghz flat-topped optical frequency comb generation", *Opt. Express*, vol. 21, no. 5, pp. 6045-6052, 2013.
- [27]T. Morioka et al. "1 tbit/s otdm/wdm transmission using a single supercontinuum wdm source", *Electronics Letters*, vol. 32, no. 10, pp. 906-907, 1996.
- [28]L. E. Hooper et al. "Coherent widely tunable source of sub-picosecond pulses using all-normal dispersion fiber continuum", 2011 7<sup>th</sup> Workshop on, pages 1-4, 2011.
- [29]S. A. Diddams et al. "Direct link between microwave and optical frequencies with a 300 THz femtosecond laser comb" *Phys. Rev. Lett.* 84, 5102-5105.
- [30]R. Trebino et al. "Measuring ultrashort laser pulses in the time-frequency domain using frequency-resolved optical gating", *Review of Scientific Instruments* 68, 3277-3295, 1997.
- [31]Jose Eduardo "Measurement of ultrashort laser pulses using the second-harmonic generation frequency-resolved optical gating", NTNU-Trondheim
- [32]S. Akturk, C. D' Amico, A. Mysyrowicz "Measuring ultrashort pulses in the single-cycle regime using frequency resolved-optical gating" *J. Optc. Soc. Am. B* Vol.23, No. 6, 2008
- [33]S. Petit, A. Telebpour A. Proulx, S.L. Chin, *Opt. Commun.* 175. 323 (2000)
- [34]J. S. Robinson, C. A. Hagworth, H. Teng, R. Smith, J. Marangos, J.W. Tisch "The generation of intense, transform-limited laser pulses with tunable duration from 6 to 30 fs in a differentially pumped hollow fiber", *Appl. Phys. B.* 85, 525-529 (2006)
- [35]F. Bohle et al. "Compression of CEP-stable multi-mJ laser pulses down to 4 fs in long hollow fibers", *Laser Phys. Lett.* 11 (2014)
- [36]T. Kanai et al. "Pointing stabilization of a high repetition-rate high-power femtosecond laser for intense few-cycle pulse generation". *Appl. Phys. Letters* 92, 061106 (2008)
- [37]F. Lucking , A. Trabboni, S. Anumula, G. Sansone, F. Calegari, M. Nisoli, T. Oksenhendler and G. Tempea "In situ measurement of nonlinear carrier-envelope phase changes in hollow core fiber compression *Opt. Lett.* 39 2302 (2014)
- [38]Czerny, M & Truner, A.F. *Z. Physik* (1930) 61:792